UNIVERSIDAD DE SONORA
DIVISIÓN DE CIENCIAS EXACTAS Y NATURALES
DEPARTAMENTO DE INVESTIGACIÓN EN FÍSICA
POSGRADO EN CIENCIAS (FÍSICA)

STUDY OF 2D MATERIALS THROUGH RAMAN SPECTROSCOPY

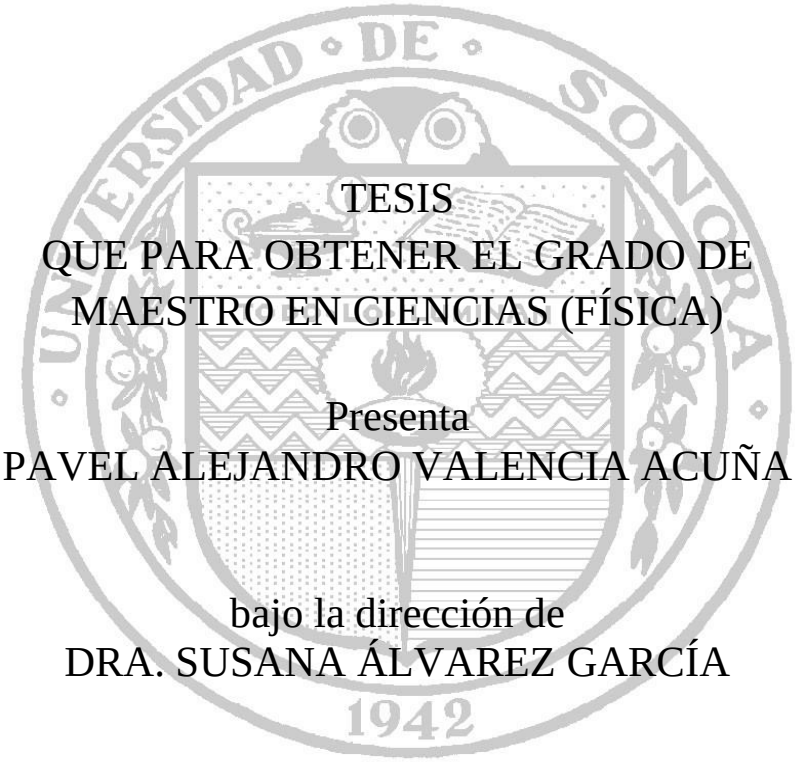

TESIS
QUE PARA OBTENER EL GRADO DE
MAESTRO EN CIENCIAS (FÍSICA)

Presenta
PAVEL ALEJANDRO VALENCIA ACUÑA

bajo la dirección de
DRA. SUSANA ÁLVAREZ GARCÍA

Hermosillo, Sonora Febrero de 2018

Universidad de Sonora

Repositorio Institucional UNISON

"El saber de mis hijos hará mi grandeza"

Thesis approval

Dr. Susana Álvarez-García

Dr. Brian LeRoy

Dr. Raúl Riera-Roche

Dr. Rafael García-Gutiérrez

Research activities performed

During this work, the following activities were carried out:

- Summer internship in the Department of Physics at the University of Arizona.
- Participation in the 21^{th} University Meeting of Research in Materials (RUIM 2017): Study of 2D materials through Raman spectroscopy.

Acknowledgment

Even though academic theses bear the name of a single author, this work would not have been possible without the mentorship and guidance of my graduate advisor, Professor Susana Álvarez-García. Prof. Álvarez-García's commitment to excellence in teaching and in research, her intellectual integrity, and his dedication to graduate students are well known to many.

I would like to thank Professor Brian LeRoy and his group, from the University of Arizona, in an emphatic way, for allow me to work in his laboratory to expand the research topic of this thesis. I likewise extend much gratitude to Alexandra Brasington and Muhed Rana, for their advice and supervision of the research done in LeRoy Group.

The esteemed members of my thesis committee, Professors Raúl Riera-Roche and Rafael García-Gutiérrez, as well as Professor LeRoy, have distinguished themselves by their supportive stance and their insightful guidance throughout my M.Sc. studies. Also, by useful discussions about the nature of the topic studied.

The National Council of Science and Technology (CONACyT), to which I express my gratitude for the trust and support that they gave me through a scholarship to pursue graduate studies at University of Sonora. I extend my thanks, promising that I will dedicate my professional life to science for humanistic purposes.

I gratefully thank my parents, Agustin and María, for their constant encouragement and wisdom, both my brother and sister, Ivan and Tania, for being a source of motivation and brightness in my life. My closest friends also have my recognition, because they were a great stimulus for my formation, not to mention their moral support.

Abstract

Two-dimensional (2D) materials are a single or a few atoms tick and self-contained in plane. Atoms are held together with covalent bond, forming sheets of material. In this work, we present an optical technique, called Raman spectroscopy, which can identify and characterize different 2D materials, as well as distinguish unambiguously the number of layers and composition. The materials under study are graphene, molybdenum disulfide (MoS2), molybdenum diselenide (MoSe2), tungsten disulfide (WS2), and tungsten diselenide (WSe2). The position, width, and intensity of the Raman bands reveals composition and structural information of the crystal.

Keywords: graphene, transitional metal dichalcogenides, 2D materials, Raman spectroscopy

Table of Contents

1. Introduction **1**

1.1. Overview……. 1

1.2. Two-dimensional materials……. 2

1.3. Producing 2D materials……... 3

1.4. Outlook……... 4

2. Theoretical framework **6**

2.1. Survey of Raman scattering……. 6

2.1.1. Quantum description of Raman scattering…… 7

2.1.2. Electron-radiation interaction……... 9

2.1.3. Electron-phonon interaction……. 9

2.1.4. Raman selection rules……... 11

2.1.5. Symmetry selection rules……. 12

2.2. Raman spectroscopy of graphene……... 12

2.2.1. Crystal structure of graphene……... 12

2.2.2. Electron in graphene…… 14

2.2.3. Phonons in graphene…… 16

2.2.4. Main bands in Raman spectra of graphene…….. 17

2.3. Raman spectroscopy of 2D TMDCs……... 23

2.3.1. Crystal structure of 2D TMDCs…….. 23

2.3.2. Electron in 2D TMDCs…… 25

2.3.3. Phonons in 2D TMDCs……... 27

2.3.4. Main bands in Raman spectra of 2D TMDCs……. 29

3. Methodology **32**

3.1. Sample…… 32

3.2. Raman spectroscopy……... 36

3.3. Data analysis……... 37

4. Experimental results **39**

4.1. Few-layers graphene……... 39

4.2. Few-layers molybdenum disulfide (MoS_2)…… 44
4.3. Few-layers tungsten disulfide (WS_2)……. 46
4.4. Few-layers molybdenum diselenide ($MoSe_2$)…… 48
4.5. Few-layers tungsten diselenide ($MoSe_2$)…… 50
5. Discussion and conclusions **52**
5.1. Discussion of few-layers graphene……. 52
5.2. Discussion of few-layers TMDCs…….. 53
5.3. Conclusion and perspectives of 2D materials…… 54
6. References **56**
A. Fitted parameters of used for graphene **61**
B. Fitted parameters used for 2D TMDCs **66**

List of Tables

2.1 The space group and the group of the wave vector point for monolayer, *N*-layer graphene and graphite at all high symmetry points. (Adapted from [19])……. 15

2.2 The space group and the group of the wave vector for *N*-layer TMDCs and bulk TMDCs at all high symmetry points. (Adapted from [25])…….. 25

2.3 Theoretical energy of the spin-orbit coupling of MoS_2, $MoSe_2$, WS_2, and WSe_2. (Adapted from [28] and [29])…… 25

3.1 Zones of interest for graphene and TMDCs. The images were captured with an objective 100x. The scales are shown for each image…….. 35

A.1 Parameters used for the fitting of T1 graphene in the range of 1300-1700 cm^{-1}... 61

A.2 Parameters used for the fitting of T2 graphene in the range of 1300-1700 cm^{-1}... 61

A.3 Parameters used for the fitting of T3 graphene in the range of 1300-1700 cm^{-1}... 62

A.4 Parameters used for the fitting of T4 graphene in the range of 1300-1700 cm^{-1}... 62

A.5 Parameters used for the fitting of T1 graphene in the range of 2300-3300 cm^{-1}... 62

A.6 Parameters used for the fitting of T2 graphene in the range of 2300-3300 cm^{-1}... 63

A.7 Parameters used for the fitting of T3 graphene in the range of 2300-3300 cm^{-1}... 64

A.8 Parameters used for the fitting of T4 graphene in the range of 2300-3300 cm^{-1}... 65

B.1 Parameters used for the fitting of T1 MoS_2…….. 66

B.2 Parameters used for the fitting of T2 MoS_2…….. 67

B.3 Parameters used for the fitting of T3 MoS_2…….. 67

B.4 Parameters used for the fitting of T1 WS_2…… 68

B.5 Parameters used for the fitting of T2 WS_2…… 68

B.6 Parameters used for the fitting of T3 WS_2…… 69

B.7 Parameters used for the fitting of T1 $MoSe_2$…… 70

B.8 Parameters used for the fitting of T2 $MoSe_2$…… 71

B.9 Parameters used for the fitting of T3 $MoSe_2$…… 72

B.10 Parameters used for the fitting of T1 WSe_2…….. 73

B.11 Parameters used for the fitting of T2 WSe_2……... 74

B.12 Parameters used for the fitting of T3 WSe_2……... 75

List of Figures

1.1 Atomic structure of single layer graphene **(a)** and single layer MX_2. **(b)**. (Adapted from [2])…….. 2

1.2 Ideal graphene **(a)**, showing a perfect lattice. Graphene with a missing atom or vacancy **(b)**. Graphene with a different atom, called impurity **(c)**. (Adapted from [9])…….……. 4

2.1 Rayleigh and Raman scattering in resonant and non-resonant condition. The Stokes and Anti-Stokes process are shown. (Adapted from [10])…… 6

2.2 Top view of the real space unit cell of monolayer graphene **(a)**. The reciprocal space unit cell showing the 1st Brillouin zone with its high symmetry points and lines **(b)**. (Adapted from [19])……..……... 13

2.3 **(a)** Electronic band structure (π electrons) and **(b)** its density of states showing the orbital contributions. (Adapted from [19] and [20], respectively)…… 14

2.4 The electronic dispersion for the π electrons, calculated by density functional theory and using the irreducible representations (Γ_π) are shown for (a) monolayer, (b) bilayer, and (c) trilayer graphene along the KΓMK directions. (Adapted from [19])……..….. 15

2.5 **(a,b)** Schematic electron dispersion of bilayer graphene along the KΓ direction showing the possible transition induced by **(a)** a photon with T_2 symmetry and **(b)** a T_1 photon. **(c)** The electronic dispersion of trilayer graphene showing the five possible transitions by light absorption. (Adapted from [19])…….… 15

2.6 Calculated phonon dispersion relation of graphene showing the LO, TO, TO, LA, TA and ZA phonon branches. The point group of the point Γ are also show (Adapted from [22])…….. 16

2.7 Graphic representation of the atomic motion of the atoms for each mode. (Adapted from [22])…… 17

2.8 Raman processes for the 2TO(K) band. Blue lines denote excitation, red line denote photon emission, and doted lines represent the wave vector of a phonon with certain energy. Triple resonance condition **(a)** and double resonance condition **(b, c)** are displayed Adapted from [23]…… 19

2.9 2TO(K) band of few-layers graphene with 2 different stacking orders under 5 different excitation energies. The intensity is normalized to the E_{2g} band intensity for each spectrum. (Adapted from [24])…… 20

2.10 Raman processes for the TO(K) band **(a, b)** and LO(Γ) band **(c, d)**. Double resonance condition is displayed in all processes. Blue lines denote excitation, red line denote photon emission, and doted lines represent the wave vector of a phonon with certain energy. The defects are displayed as horizontal doted lines. (Adapted from [23])…….. 22
2.11 Raman processes for the TO(K)+LA(K) band **(a)** and 2LO(Γ) band **(b)**. Double resonance condition is displayed in all processes. Blue lines denote excitation, red line denote photon emission, and doted lines represent the wave vector of a phonon with certain energy. The defects are displayed as horizontal doted lines. (Adapted from [23])…….. 23
2.12 **(a)** Transition metal atom coordination for trigonal prismatic polytype. The blue spheres represent transition metal atoms and orange ones, chalcogen atoms. **(b)** Top view of 2D TMDCs with its unit cell marked in the black rhombus. **(c)** Top view of 2D TMDCs with its primitive unit vectors. (Adapted from [25])…… 24
2.13 Electronic band structure without SOC of **(a)** MoS_2 and **(b)** WS_2 with its density of states. The energy of the band gap is displayed in both cases. (Adapted from [30])……**....** 25
2.14 Electronic band structure with SOC of **(a)** monolayer, and **(b)** bilayer MoS_2, $MoSe_2$, WS_2, and WSe_2. Direct to indirect transition is displayed. (Adapted from [27])……**...** 27
2.15 Phonon for 1L-MoS_2 showing the optical and acoustic branches. (Adapted from [32])……... 28
2.16 Phonon dispersions for **(a)** 1L-WS_2, **(b)** 1L-$MoSe_2$ and **(c)** 1L-WSe_2. (Adapted from [32])…….. 29
2.17 Graphic representation of the atomic motion of the metal (M) and chalcogens (X) atoms for each mode. (Adapted from [32])…….…… 29
2.18 Dependence of the bands of MoS_2 on the laser energies. The 2LA band was assigned for the M point in this case. (Adapted from [22])……..…… 31
3.1 Scotch tape method. (Adapted from [1])……..… 33
3.2 Image of the sample with an objective of 10x **(a)** and 100x **(b)**. The setup for capturing the image is also shown **(c)**……..…… 34
3.3 Raman microscopy setup. M stand for mirror, SNF for single-notch filter, and OBJ for objective…….…... 36
3.4 **(a)** Optical image of MoS_2 under a 100x objective, where the blue point indicates the focus of the laser spot. **(b)** Raman plot obtained from the point A. 37
4.1 Raman spectrum of few-layers graphene of the points T1, T2, T3 and T4…..… 39

4.2 Fitted curves (red) with the data (black points) along with the residual (green) and its cumulative fitting curve (magenta) for the E2g and 2TO(K) bands at points: **(a, b)** T1, **(c, d)** T2, **(e, f)** T3, and **(g, h)** T4, in few-layers graphene. Coefficient of determination (R^2) is shown for each case…… 40
4.3 Fitted curves (red) with the data (black points) along with the residual (green) and its cumulative fitting curve o (magenta) for the TO(K) band at point T1….. 42
4.4 Fitted curves (red) with the data (black points) along with the residual (green) and its cumulative fitting curve o (magenta) for the TO(K)+LA(K) and 2LO(Γ) bands at points: **(a, b)** T1, **(c, d)** T2, **(e, f)** T3, and **(g, h)** T4, in few-layers graphene. Coefficient of determination (R^2) is shown for each case…… 43
4.5 Raman spectrum of few-layers MoS_2 of the points T1, T2, and T3……. 44
4.6 Fitted curves (red) with the data (black points) along with the residual (green) and its cumulative fitting curve o (magenta) for the points: **(a)** T1, **(b)** T2, and **(c)** T3, for few-layers MoS_2…….……... 45
4.7 Raman spectrum of few-layers WS_2 of the points T1, T2, and T3…….…… 46
4.8 Fitted curves (red) with the data (black points) along with the residual (green) and its cumulative curve of the adjust (magenta) for the points: **(a)** T1, **(b)** T2, and **(c)** T3, for few-layers WS_2……..…. 47
4.9 Raman spectrum of few-layers $MoSe_2$ of the points T1, T2, and T3…… 48
4.10 Fitted curves (red) with the data (black points) along with the residual (green) and its cumulative curve of the adjust (magenta) for the points: **(a)** T1, **(b)** T2, and **(c)** T3, for few-layers $MoSe_2$……... 49
4.11 Raman spectrum of few-layers WSe_2 of the points T1, T2, and T3……. 50
4.12 Fitted curves (red) with the data (black points) along with the residual (green) and its cumulative curve of the adjust (magenta) for the points: **(a)** T1, **(b)** T2, and **(c)** T3, for few-layers WSe_2……..…… 51

1. Introduction

1.1. Overview

Over the past years, advances in modern technology relies in the miniaturization of devices, such as thin films, which are reduced to fractions of nanometers to several micrometers thickness. Products such as semiconducting lasers or light emitting diodes relies on the deposition of thin films to transform materials on functional devices. Nevertheless, the active area is permanently attached to a substrate, which serves just as a mechanical support.

An emerging class of thin films are the two-dimensional (2D) materials. They are a single or few atoms thick and self-contained in plane. Atoms are held together with strong covalent bond, forming sheets of material. When placed over a bulk surface or another 2D material, the interaction is governed by van der Waals forces. Those forces are relatively weak, making possible to detach layers from bulk material.

2D materials act as discrete "building blocks". This property suggests the possibility of stacking them to create functional materials. Such materials would be designed depending on the chemical composition of each layer of material. The most familiar example of a 2D material is graphene, and since its exfoliation from graphite, it set in motion an interest in atomically thin materials for both fundamental research and device application.

This dissertation addresses a characterization technique for those building blocks, which can vary spatially because of their composition and structure. We present an optical tool, which can identify and characterize many different 2D materials, as well as distinguish unambiguously the number of layers and composition. In the present chapter, we review the current *state of art* of 2D materials, focusing on graphene and the semiconducting family of transition metal dichalcogenides. We will include a summary of their properties as well. The direction of this thesis towards 2D materials is presented in the concluding section.

1.2. Two-dimensional materials

Graphene, the subject of the 2010 Nobel Prize in Physics [1], is a single-atom thick layer of carbon atoms arranged in a honeycomb lattice (Figure 1.1.a). It is the most studied 2D material, and because of its band structure, it is considered a special kind of semimetal with extremely high carrier mobility and peculiar electrical transport behavior. Graphene has a zero bandgap and a linear energy dispersion relation, which are useful in many parctial applications. Although, graphene was the first 2D material to be realized, other materials exist in the form of layers.

Another group of 2D materials is the transition metal dichalcogenides (TMDCs), which consist of a MX_2 structure, in which M is a transition metal and X is a chalcogen atom. In TMDCs, two adjacent sheets of chalcogen atoms are separated by one of transition metal atoms (Figure 1.1.b) in a X-M-X configuration, making its building block composed of an atomic trilayer structure. TMDCs offers properties that complement those of graphene; they display a band gap of the order of 1-2 eV and show electron mobilities comparable to those of silicon. Intensive research efforts on TMDCs optoelectronics have started merely 6 years ago and have already lead to some exciting and promising new developments. Particularly, we focus on the semiconducting transition metal dichalcogenides MoS_2, $MoSe_2$, WS_2, and WSe_2 due to their inertness and stability in ambient conditions like graphene.

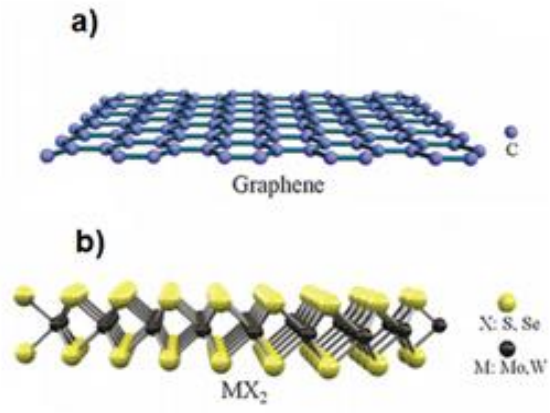

Figure 1.1: Atomic structure of single layer graphene **(a)** and single layer MX_2. **(b)**. (Adapted from [2]).

The fundamental physics of single- and few-layer sample was the initial focus of early studies of 2D materials. Physical properties of these materials differ from their bulk counterpart. In TMDCs, layer-dependent indirect-direct bandgap transition was observed, which resulted in bright photoluminescence (PL) from monolayers [3]. PL from bulk crystals, on the other hand, was found to be practically absent. In the case of graphite (bulk) and graphene (layer), the first is naturally a very brittle compound, and the second is the strongest material ever recorded [4].

1.3. Producing 2D materials

The first method used to isolate 2D materials, such as graphene, was the "scotch tape method". It mechanically exfoliates layers (repeated peeling) of higher pyrolytic graphite and deposited on an arbitrary substrate, typically on Si/SiO_2. This method enables to produce high quality samples, but it is limited to small samples of lateral dimensions around 20 μm [5]. Even though this method enables high quality samples, it is not scalable and high time consuming.

For viable technological application, it necessary to be able to produce large areas samples. Chemical vapor deposition (CVD) is a technique for synthesizing a variety of 2D materials of considerable size [6]. This process involves heating a substrate in an insolate furnace and a flowing precursor gas, which fall apart and deposits material onto the substrate. Proper choice of substrate, temperature, and flow of gas differs from the material that will be grow. For example, copper is the ideal growth substrate for graphene [7]. As for TMDCs, the process is not as well established as that of graphene, but currents make possible to grow TMDCs on wafer scale [8].

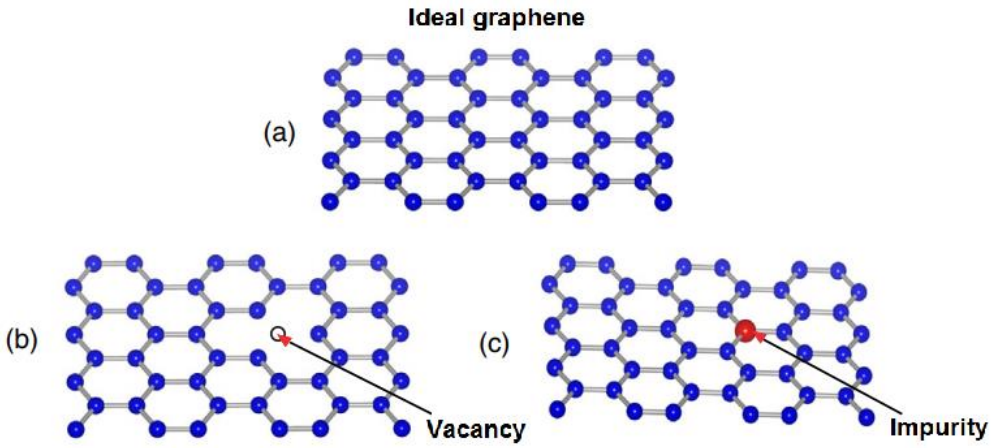

Figure 1.2: Ideal graphene **(a)**, showing a perfect lattice. Graphene with a missing atom or vacancy **(b)**. Graphene with a different atom, called impurity **(c)**. (Adapted from [9]).

The structure of 2D materials can contain vacancies or substitutional impurities (see Figure 1.2). Those defects on the sample are introduced unintentionally during the process of growth when conditions are not ideal. Defects can also be introduced intentionally to control the density of free carriers. Surveying the presence of defects on the sample is required to evaluate a technique of grow.

1.4. Outlook

As mentioned above, unique structural features and compositional variations exist in 2D material. It is crucial that we understand the structure and local composition of these materials and stablish a relationship between structural features and the properties of the material. Hereafter, we present an optical technique for monitoring the defects, grain boundaries, number and orientation of layers.

In chapter 2 we review the theoretical framework corresponding to the physical definition of the materials we study; crystal structure and phonon dispersion. Later, in the same chapter, we discuss the scattering of photons by phonons. Raman spectroscopy is a technique, collects the scattered photons to probe the phonon band structure of materials, which change depending on the kind of material and the unique features mentioned above.

The methodology of this work is presented in chapter 3. First, we show the methods used to produce 2D materials. Later, the technique of characterization, which is an optical set up for Raman microspectroscopy. Finally, the approach used for the data acquisition and its handling are presented.

As for the results of the techniques used, presented in chapter 4, we will see that the information given from this approach, helps us to gain an understating of the physical structure of the sample studied. Chapter 5 will include a discussion and conclusion of this work, as well as its future direction, which are methods of improving the monitoring process in time and resolution. This enhance will raise insights about the additional features presented in samples from the CVD technique, which are summarized in the same chapter.

2. Theoretical framework

2.1. Survey of Raman scattering

Raman scattering [10] is the inelastic scattering of the radiation by the vibration of the material. When the radiation, or a photon impact on a sample, it creates a time-dependent perturbation of the Hamiltonian. This perturbation introduced by a photon of energy $\hbar\omega_L$ is known as the electron-radiation interaction and it increases the total energy to $E_g + \hbar\omega_L$, where E_g is the ground state energy. In general, $E_g + \hbar\omega_L$ does not correspond to a real state, therefore the system is said to be in a virtual level. Classically, this correspond to a forced oscillation of the electrons with frequency ω_L. The photon leaves this unstable situation and we can formally consider as being emitted by the perturbed system, making it to a real state.

Depending on the initial and final state of this process, it can be further classified (see Figure 2.1). When the system returns to its initial state, and the energy of the emitted (scattered) photon remains the same as the incident one, it is called *Rayleigh scattering* or *elastic scattering*. Regardless of the null change, this scattered radiation can give useful information [11, 12].

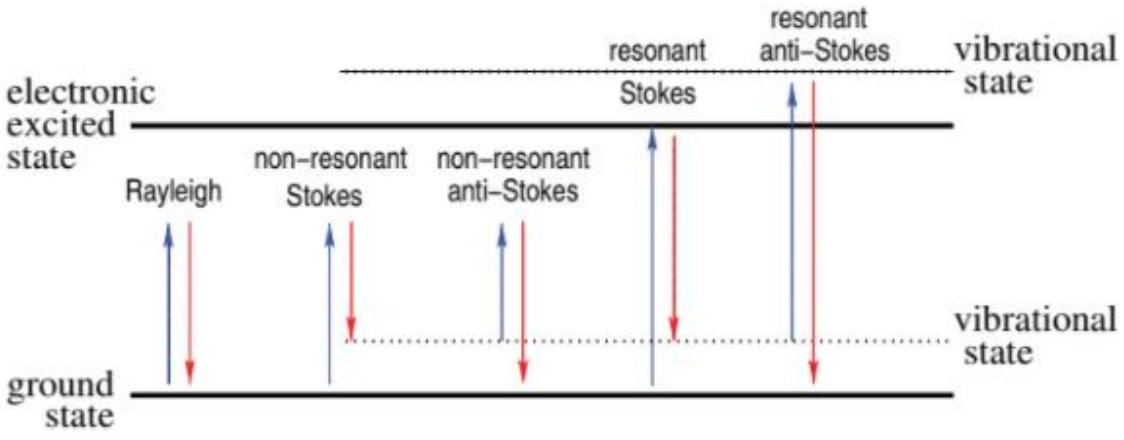

Figure 2.1 Rayleigh and Raman scattering in resonant and non-resonant condition. The Stokes and Anti-Stokes process are shown. (Adapted from [10]).

Raman scattering occurs when the photon loses or gain energy in the interaction process, thus making a change in the frequency of the photon of energy $\hbar\omega_{Sc}$. The energy loss must correspond to a phonon energy of $\hbar\omega_L - \hbar\omega_{Sc} = \hbar\Omega$, corresponding to the Stokes process. The incoming radiation can also gain energy if the photon finds the sample in an excited vibrational state, and after the interaction the systems return to its ground state, leaving with an increased energy $\hbar\omega_{Sc} = \hbar\omega_L + \hbar\Omega$. This corresponds to the Anti-Stokes process. At room temperature, the Stokes process is the most probable [14], since vibrations on matter (phonons) are related to the temperature of it.

Additionally, if $E_g + \hbar\omega_L$ if correspond to a real state, it will be called *resonant* Raman scattering. Otherwise, it will be called normal or *non-resonant* Raman scattering. When the process is *resonant*, the intensities are enhanced, because of a greater perturbation efficiency. In the quantum mechanical description, this correspond to a vanishing denominator in the perturbation theory expression.

In general, Raman scattering can be described in the framework of classical electromagnetism, considering the polarizability of a material in response of an incident oscillating electric filed. This description allows to explain the major features of most Raman spectra: Stokes and Anti-Stokes processes, Raman lineshape, momentum and energy conservation selection rules. However, the classical treatment fails in the quantitative description of the Raman intensities and that of the resonance Raman scattering process which occurs particularly in graphene. Because of its importance, we limited us to the quantum description[1] of the Raman process.

2.1.1. Quantum description of Raman scattering

Quantum description of Raman scattering response of a material involve the solution of the Schrödinger equation with an external field given by a sinusoidal function of time. Considering that the external electromagnetic fields are sufficiently weak, the problem can be solved by time-dependent perturbation theory. Detailed development can be found in [15].

1) This approach, although called quantum, it is considered semiclassical, because we are describing the interaction of light with matter in terms of a classical electromagnetism field perturbing a quantum mechanical system.

For a general scattering process involving an *n*-phonon process, we have an $(n+2)$ order matrix of the transition amplitude:

$$\mathcal{M} = \sum_{s_0,\dots,s_n} \frac{\langle f|\hat{H}_{er}|s_n\rangle\langle s_n|\hat{H}_{ep}|s_{n-1}\rangle \dots \langle s_1|\hat{H}_{ep}|s_0\rangle\langle s_0|\hat{H}_{er}|i\rangle}{(\hbar\omega_L - E_n + i\Gamma_n/2) \dots (\hbar\omega_L - E_1 + i\Gamma_1/2)(\hbar\omega_L - E_0 + i\Gamma_0/2)} \tag{2.1}$$

with $|i\rangle$ the initial state, $|f\rangle$ the final state. s_k $k = 0, 1, 2, \dots, n$ label the intermediate states where no photons are present, but an electron-hole pair is created, and *k* photons emitted. E_k and $\Gamma_k/\hbar$ are the energies and decay rated of the intermediate states. $\hat{H}_{er}$ and $\hat{H}_{ep}$ are the Hamiltonian operators describing the interaction of the electron-radiation and electron-phonon, respectively. The form of those Hamiltonian will be discussed in the next section.

Given $\mathcal{M}$, one could sum its square over the phonon wavevectors $\boldsymbol{q}$ with fixed total energy, to obtain the frequency-resolved intensity $I(\omega)$:

$$I(\omega_{Sc}) \propto \int |\mathcal{M}|^2 \delta\left(\Omega_{q_1}^{\nu_1} + \dots + \Omega_{\boldsymbol{q_n}}^{\nu_n} - \omega_{Sc}\right) d^2\boldsymbol{q_1} \dots d^2\boldsymbol{q_n} \tag{2.2}$$

where $\boldsymbol{q_1}, \dots, \boldsymbol{q_n}$ are the wave vectors of the emitted phonons, $\nu_1, \dots, \nu_n$ their branch labels, and $\Omega_{\boldsymbol{q_1}}^{\nu_1}, \dots, \Omega_{\boldsymbol{q_n}}^{\nu_n}$ are their frequencies. For dispersionless undamped phonons, Ω^{ν}, the shape of the n-phonon peak is $\propto \delta(n\Omega^{\nu} - \omega_{Sc})$ with zero width, infinite height, but well-defined area. If the phonons can decay due to anharmonicity [16] or electron-phonon coupling [17], the peak is broadened into a Lorentzian, but the area is preserved. If phonon have a weak dispersion, then states with different momenta contribute at slightly different frequencies, resulting in an overall shift and non-trivial peak shape, frequency integration across the peak means counting all phonon states. This is written as:

$$A = \int\limits_{\omega_{Sc} \in \text{peak}} I(\omega_{Sc}) d\omega_{Sc} \propto \int |\mathcal{M}|^2 \, d^2\boldsymbol{q_1} \dots d^2\boldsymbol{q_n} \, . \tag{2.3}$$

2.1.2. Electron-radiation interaction

The electron-radiation term $\widehat{H}_{er}$ can be obtained from the quantum mechanical Hamiltonian describing the motion of a charge $-e$ in an external electromagnetic field, given by:

$$H = \frac{1}{2m}(\boldsymbol{p} - e\boldsymbol{A})^2 + V(\boldsymbol{r})\,, \tag{2.4}$$

where m and e are the electron mass and charge, $\boldsymbol{p}$, $\boldsymbol{A}$, and $V(\boldsymbol{r})$ are the momentum, vector potential and crystal potential. In the Coulomb gauge, equation 2.4 becomes

$$H = \left[\frac{p^2}{2m} + V(\boldsymbol{r})\right] - \frac{e}{m}\boldsymbol{p}\cdot\boldsymbol{A} + \frac{e^2}{2m}A^2\,. \tag{2.5}$$

The term in brackets gives the Hamiltonian for an electron in the potential $V(\boldsymbol{r})$. Additionally, in the weak field approximation, the A^2 term can be neglected. The electron-radiation interaction is given by the extra term as

$$H_{er} = -\frac{e}{m}\boldsymbol{p}\cdot\boldsymbol{A}\,. \tag{2.6}$$

For light scattering by a crystal, the wavelength of the electromagnetic radiation is much larger than the dimensions of the unit cell. Also, an electron basis wavefunction $\varphi(\boldsymbol{r})$ is localized around the position of an atom $\boldsymbol{r}_0$. Considering monochromatic plane waves ($\boldsymbol{A}(\boldsymbol{r},t) \propto e^{i\boldsymbol{k}\cdot\boldsymbol{r}}$), the interaction Hamiltonian can be considered within the dipole approximation, which is represented by

$$H_{er} = -e\boldsymbol{r}\cdot\boldsymbol{E}(\boldsymbol{r_0},t) \tag{2.7}$$

2.1.3. Electron-phonon interaction

With the Born-Oppenheimer approximation[2], we can decompose the Hamiltonian of a crystal in three terms:

$$\widehat{H}_{crystal} = \widehat{H}_p + \widehat{H}_e + \widehat{H}_{ep} \tag{2.7}$$

2) The Born-Oppenheimer approximation, also known as adiabatic approximation, neglects the motion of the atomic nuclei when describing the electrons in a material. The physical basis for this is the fact that the mass of an atomic nucleus is much larger than the mass of the electron.

where $\hat{H}_p$ is the Hamiltonian describing the ionic motion under the influence of the ionic potentials plus the time-averaged adiabatic electronic potentials. $\hat{H}_e$ is the Hamiltonian for the electrons with the ions frozen in equilibrium position, and $\hat{H}_{ep}$ describes the change in the electronic energy as a result of the displacements of the ions from their equilibrium position. $\hat{H}_{ep}$ is known as the electron-phonon interaction and is responsible for the electrical resistance in reasonably pure semiconductors at room temperature.

Within the spirit of the Born-Oppenheimer approximation, we assume that the electrons can respond instantaneously to the ionic motion so that the electron-phonon interaction Hamiltonian can be expressed as a series around its equilibrium position $\boldsymbol{R}_{j0}$ of the electronic Hamiltonian $\hat{H}_e$:

$$\hat{H}_{ep} = \sum_j \left(\frac{\partial \hat{H}_e}{\partial \boldsymbol{R}_j}\right)\Big|_{\boldsymbol{R}_{j0}} \cdot \delta \boldsymbol{R}_j + \cdots \tag{2.8}$$

Usually, the electronic Hamiltonian is not known, and therefore approximations are needed to calculate the electron-phonon interaction. If the electronic energies of a non-degenerate band $E_{n\boldsymbol{k}}$ (where n is the band index and $\boldsymbol{k}$ the wave vector) are known so that the expectation value of $\left(\partial \hat{H}_e / \partial \boldsymbol{R}_j\right)$ can be approximated by

$$\left(\frac{\partial \hat{H}_e}{\partial \boldsymbol{R}_j}\right)\Big|_{R_{j0}} \cdot \delta \boldsymbol{R}_j \approx \left(\frac{\partial E_{nk}}{\partial \boldsymbol{R}_j}\right)\Big|_{\boldsymbol{R}_{j0}} \cdot \delta \boldsymbol{R}_j \,. \tag{2.8}$$

The constant $\left(\partial E_{nk} / \partial \boldsymbol{R}_j\right)$ represents simply the shift of the electronic band energy caused by a static displacement of the atoms. Those displacements can correspond to a deformation of the crystal which will change the electronic energies; the parameters which describe these changes in the electronic energies induced by static distortions of the lattice are known as deformation potentials.

2.1.4. Raman selection rules

If $\boldsymbol{k}_L$ and $\omega_L = ck_L$ are the wave vector and frequency of the incoming photon, $\boldsymbol{k}_{Sc}$ and $\omega_{Sc} = ck_{Sc}$ those of the scattered photon, with c being the speed of light, then energy and momentum conservation give:

$$\omega_L = \omega_{Sc} \pm \Omega_{\boldsymbol{q}}^{\nu} \,, \tag{2.9}$$

$$\boldsymbol{k}_L = \boldsymbol{k}_{Sc} \pm \boldsymbol{q} \,. \tag{2.10}$$

When a phonon is created (‘‘+’’), it belongs to the Stokes process, and in the Anti-Stokes process is annihilated (‘‘-’’). Typical Raman experiments are conducted in the visible range of spectrum corresponding to (400-600 nm). Since the lattice parameter, a, is of the order 0.1 nm, $k_L, k_{Sc} \ll \pi/a$, the magnitude of a zone boundary wavevector. From (2.9) and (2.10), $q \ll \pi/a$, i.e. only phonon with $\boldsymbol{q} \approx 0$ are measured in first-order scattering (1-phonon process). This is the *fundamental Raman selection rule.* Phonon momentum with $\boldsymbol{q} \neq 0$, will become important in defect-induced or higher-order Raman scattering processes. The order of the Raman process is given by the number of scattering events that are involved in the Raman process

However, in the case of a 2-phonon process (second-order), the emission of two phonon with opposite wavevectors can always satisfy the fundamental selection rule: $\boldsymbol{q} + (-\boldsymbol{q}) = 0$. For two different phonons, the peaks are referred as the *combination* of modes. If the two phonons are identical, the resultant is called an *overtone*. Since each individual phonon has no restriction of the individual phonon wavevector as there is in the 1-phonon process, all phonon may contribute to a multi-phonon process.

The overtone Raman spectrum, after dividing the Raman frequency by two, is a measure of the phonon density of states (PDOS), modified by a factor dependent of the phonon occupancy and scattering efficiency. Second-order Raman scattering is usually much weaker than first-order scattering (third-order being weaker than second-order, and so on), but will be resonantly enhanced by the interband transition of a semiconductor. This enhancement makes it possible to detect the phonons with $\boldsymbol{q} \neq 0$ [18].

2.1.5. Symmetry selection rules

The symmetry selection rules result from the conditions to get a not vanish value of the matrix elements between some interaction Hamiltonian H' that coupled two states $|\alpha\rangle$ and $|\beta\rangle$: if $H'|\beta\rangle$: is orthogonal to$|\alpha\rangle$:, then the matrix element $\langle\alpha|H'|\beta\rangle$ vanishes. Group theory allows to evaluate whether the matrix elements vanishes or not. The process is as follows: first we identify the Irreducible Representations (IRs) for H', $|\alpha\rangle$ and $|\beta\rangle$**.** Then we multiply the characters of H' and $|\beta\rangle$ IR. The multiplication result will be described by a linear combination of characters coming from different IRs of the group. If this linear combination contains the IRs corresponding to the $|\alpha\rangle$ states, then the matrix element is non-vanishing.

2.2. Raman spectroscopy of graphene

2.2.1. Crystal structure of graphene

A hexagonal lattice of sp^2-hybridized carbon atoms is the fundamental crystal structure of graphene. Modeled with planar structure based on a unit cell of two carbon atoms A and B, and primitive lattice vectors given by

$$\boldsymbol{a_1} = a\left(\frac{\sqrt{3}}{2}, \frac{1}{2}, 0\right) \qquad \boldsymbol{a_2} = a\left(\frac{\sqrt{3}}{2}, -\frac{1}{2}, 0\right) \tag{2.11}$$

where $a = 0.1421\ nm$ is the carbon-carbon, or nearest-neighbor distance. These primitive vectors are shown in Figure 2.1.a and they serve to localize all carbon atoms of the crystal structure. In the reciprocal lattice, the primitive vectors are given by

$$\boldsymbol{b_1} = \frac{2\pi}{\sqrt{3}a}\left(1, \sqrt{3}, 0\right) \qquad \boldsymbol{b_2} = \frac{2\pi}{\sqrt{3}a}\left(1, -\sqrt{3}, 0\right). \tag{2.12}$$

The three high symmetry points of the Brillouin zone[3], Γ, K and M are the center, the corner, and the center of the edge of the hexagon, respectively, as shown in Figure 2.1.b. Other high symmetry points or lines are along ΓK (named T), KM (named T′) and ΓM (named Σ). The groups for wavefunction at the k point in the Brillouin zone are usually named the *group of the wave vector*.

3) The Brillouin zone is an abstract concept. This zone exists in a space defined by the wave vectors and the energy of the electron.

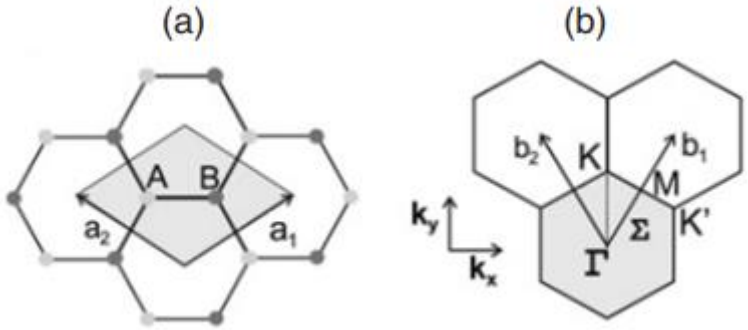

Figure 2.2 Top view of the real space unit cell of monolayer graphene **(a)**. The reciprocal space unit cell showing the 1st Brillouin zone with its high symmetry points and lines **(b)**. (Adapted from [19]).

Monolayer graphene is an isotropic planar medium described by the 2D space group $P6/mm$. The main symmetry operation distinguishing the point group between even and odd number of layers (*N = 1, 2, 3, …*) is the horizontal mirror plane symmetry, which is absent for *N* odd. The space group, and the group of the wave vector for all the high symmetry points and lines for monolayer graphene, even and odd layers (*N > 1*), and for graphite in the large N limit are listed in Table 2.1. The point u have no special symmetry operations. The group of the wave vector for *N*-layers graphene are subgroups of the one for single-layer graphene.

Table 2.1 The space group and the group of the wave vector point for monolayer, *N*-layer graphene and graphite at all high symmetry points. (Adapted from [19])

	Γ	**K(K')**	**M**	**T(T')**	**Σ**	**u**
Monolayer	D_{6h}	D_{3h}	D_{2h}	C_{2v}	C_{2v}	C_{1h}
N even	D_{3d}	D_3	C_{2h}	C_2	C_{1v}	C_1
N odd	D_{3h}	C_{3h}	C_{2v}	C_{1h}	C_{2v}	C_{1h}
N infinite	D_{6h}	D_{3h}	D_{2h}	C_{2v}	C_{2v}	C_{1h}

2.2.2. Electrons in graphene

In the case of graphene, the conduction and valence bands meet at the K point (see Figure 2.3a), making a linear dispersion around this point for the energy of the electrons. Its contribution comes mostly, as shown by a density of states (DOS) from the electrons in the p_z orbitals, as shown in Figure 2.3b. It is in fact, this p_z electron that gives graphene its excellent properties.

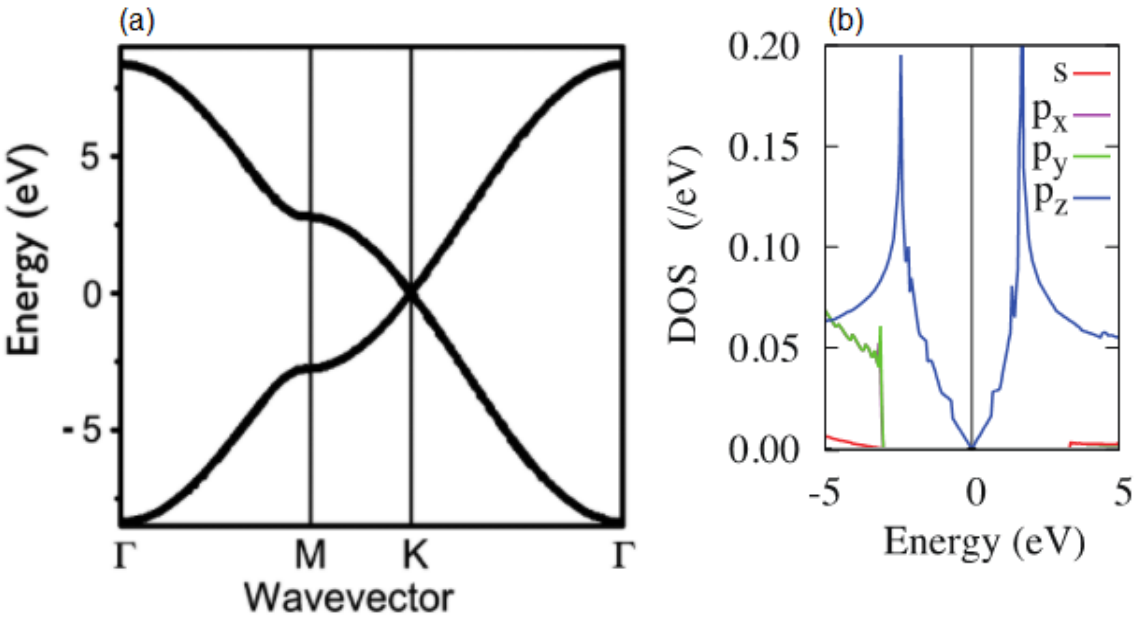

Figure 2.3 (a) Electronic band structure (π electrons) and (b) its density of states showing the orbital contributions. (Adapted from [19] and [20], respectively).

When joining graphene sheets to form a bilayer or a trilayer graphene with the Bernal stacking structure (AB for bilayer, ABA for trilayer, and so on), the unit cell will be formed by four and six atoms, respectively. Therefore, the bands will split into symmetric and antisymmetric combinations of graphene electronic states. Figure 2.4 shows the electronic dispersion of the π electrons for monolayer, bilayer, and trilayer graphene. All the bands show the elements of the IR of the wavevector point group.

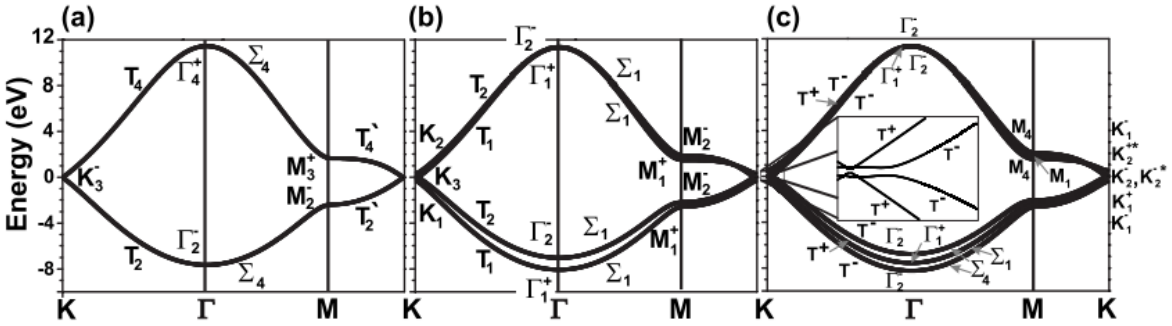

Figure 2.4 The electronic dispersion for the π electrons, calculated by density functional theory and using the irreducible representations (Γ_π) are shown for (a) monolayer, (b) bilayer, and (c) trilayer graphene along the KΓMK directions. (Adapted from [19]).

Light absorption up to 3 eV occurs mostly along the T, T' lines. There is some absorption at general points near the K(K') point in the case of graphene [19]. The allowed processes for the electron-phonon scattering for single, bilayer, and trilayer graphene are shown in Figure 2.5. Knowing the symmetries of these bands, we can know the possible transitions. Bilayer graphene contain four electronic bands along the T line, while trilayer graphene have six of them around the same line. The number of possible transition will be four for the bilayer and five for the trilayer. A detailed group theory analysis of the electrons in graphene can be found in [21].

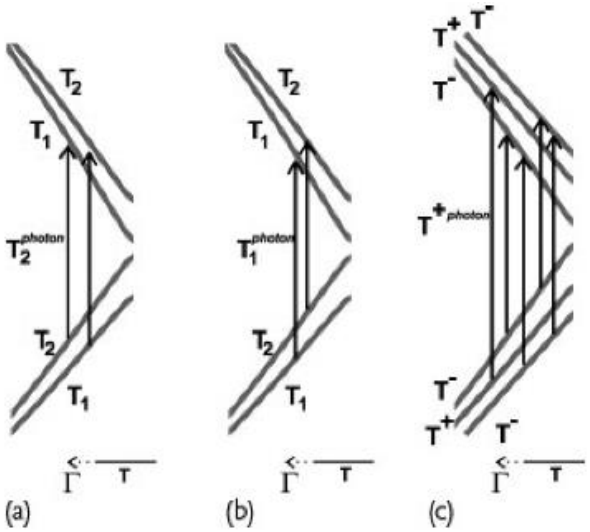

Figure 2.5 (a,b) Schematic electron dispersion of bilayer graphene along the KΓ direction showing the possible transition induced by **(a)** a photon with T_2 symmetry and **(b)** a T_1 photon. **(c)** The electronic dispersion of trilayer graphene showing the five possible transitions by light absorption. (Adapted from [19]).

2.2.3. Phonons in graphene

There are six branches in the phonon dispersion relations $\omega(\boldsymbol{q})$ because the crystal has a unit cell with two distinct atoms sites. Three are acoustic branches (A) and the other three are optic (O) phonon branches. For one acoustic branch (A) and one optic (O) phonon branch, the atomic vibrations are perpendicular to the graphene plane, and they correspond to the out-of- plane (Z) phonon modes. For two acoustic and two optic phonon branches, the vibrations are in-plane. Also, the phonon modes are classified as longitudinal (L) or transverse (T) according to vibrations parallel with or perpendicular to the plane. The phonon dispersion of monolayer graphene can be calculated by density functional theory within the local density approximation [19].

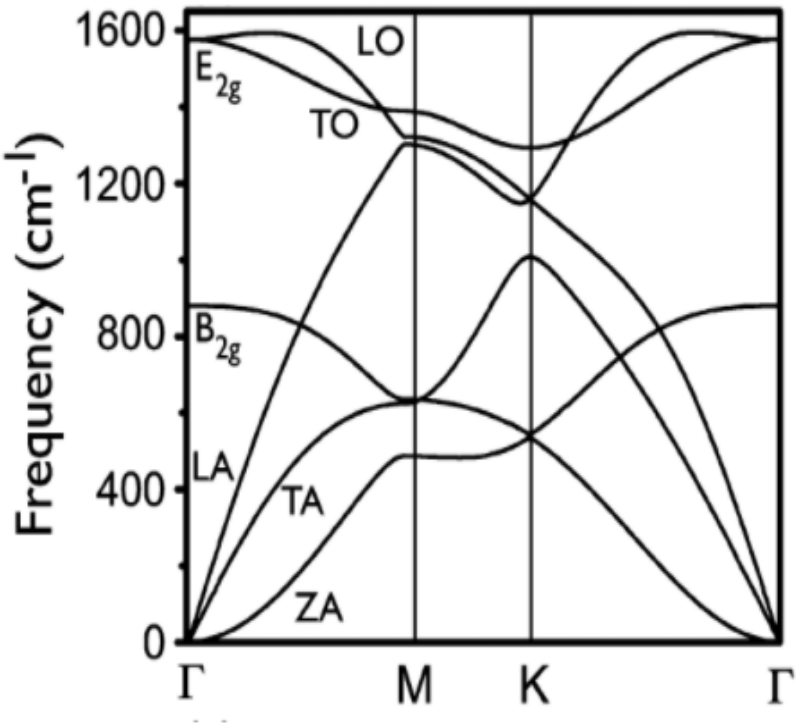

Figure 2.6 Calculated phonon dispersion relation of graphene showing the LO, TO, TO, LA, TA and ZA phonon branches. The point group of the point Γ are also show (Adapted from [22]).

The eigenvectors in graphene, which represent the movement of the atoms in the crystal, consist of three translations of the crystal along x, y, z, which have no restoring force,

making them phonons with zero frequency (LA, TA and ZA). The rest are vibrational modes, as shown in Figure 2.7. A very small splitting of the branches of monolayer is expected with increasing the number of layers because of increasing atoms in the unit cell. This split is small because the van der Waals interlayer interaction is weak [19].

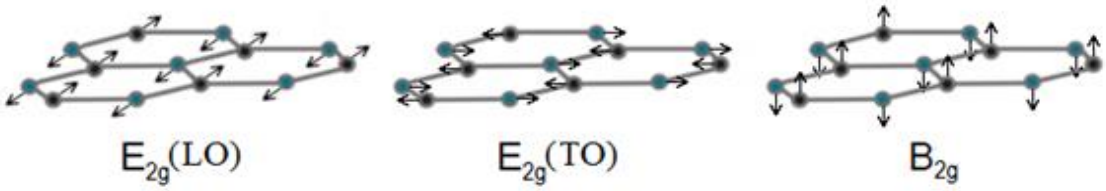

Figure 2.7 Graphic representation of the atomic motion of the atoms for each mode. (Adapted from [22]).

Although there are three optical modes at the Γ point, two are degenerate and one is not Raman-active (B_{2g} mode). The first-order Raman spectra is therefore composed of a single band, which is double degenerate at the Γ point with E_{2g} symmetry. The first-order Raman-active modes for *N* layer graphene (*N* > 1) are:

$$\Gamma^{Raman} = N\left(E_g + A_{1g}\right), \text{ for } N \text{ even}$$
$$\Gamma^{Raman} = NE' + (N-1)(E'' + A'_1), \text{ for } N \text{ odd.} \quad (2.13)$$

As mention in section 2.2.1, the Raman-active modes show symmetry variation depending on the number of layers.

2.2.4. Main bands in Raman spectra of graphene

The normal notation to assign each band in Raman scattering is by naming it as their point group symmetry. The first notation used to describe the bands in the Raman spectra of graphene were the G band (first-order band) and the G´ (second order band). This notation causes a lack of a precise physical meaning; thus, we will be using the representation of the point group notation for bands originating from 1-phonon process (Γ point). For higher-order bands, the notation of their phonon branch contribution around certain point in the Brillouin zone is used.

E_{2g} band

This band is a 1-phonon process that appears at ~1585 cm^{-1} and it is related to the in-plane motions of the C-C bond stretching modes (see Figure 2.7). Due to the strong bonding and small mass of the carbon atoms, this band has a relatively high Raman frequency. It is associated with the doubly degenerate phonon modes TO and LO at the Γ point. This is since the hexagonal symmetry of the graphene structure allows a non-dependence on the vibration direction in the *xy*-plane. In the old notation this band is, is referred as the G band (from Graphite).

This band is sensitive to strain, external charges, and doping. When graphene is uniaxially strained, the degeneracy is broken (the hexagonal symmetry is broken), making this band split in two bands (E_{2g}^{+} and E_{2g}^{-}), associated with vibrations parallel and perpendicular to the strain direction [19]. The presence of external charges and doping cause a change in position and line width, making possible to characterize these external factors in the sample [23].

Increasing the number of layers of graphene change the point group symmetry and its representation. Nonetheless, in all bibliography, despite this change in symmetry, the band is still called as in the point group of the building block (monolayer graphene). We will use this convention as well to make more convenient and save notation for the evolution of this band while increasing the thickness.

2TO(K) Band

In early studies, the only bands seen in sp^2 carbon materials were the E_{2g} band and another around ~2700 cm^{-1}. This band was called G' (also from Graphite) in the old notation, but as mention above, we will call it 2TO(K) band. It is associated with two phonons of the TO band around K, making a intervalley scattering from K to K'. It a second-order 2-phonon process and its exhibits a frequency dependence on the laser excitation energy.

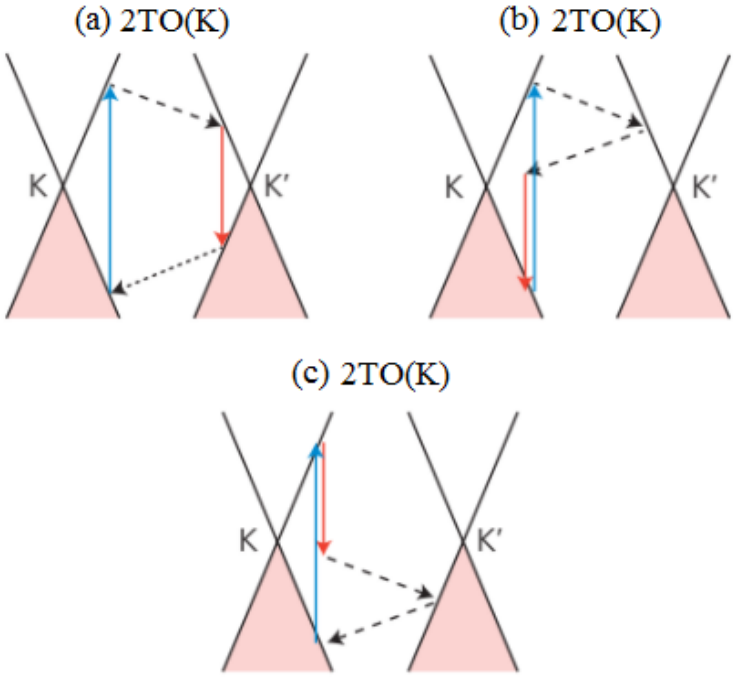

Figure 2.8 Raman processes for the 2TO(K) band. Blue lines denote excitation, red line denote photon emission, and doted lines represent the wave vector of a phonon with certain energy. Triple resonance condition **(a)** and double resonance condition **(b, c)** are displayed Adapted from [23]

For 2-phonon processes, the fundamental selection rule can be obeyed by any pair of phonons with opposite wavevectors. Since the graphene electronic energy band does not have a gap, the wave vector for any laser satisfies the resonance condition (see section 2.1). Additionally, depending on the number of vanishing factors in the denominator of (2.1), the process can be classified as double or triple resonant[4] (see Figure 2.8). The high intensity of this peak compared to the first-order peak was attributed to this effect [19].

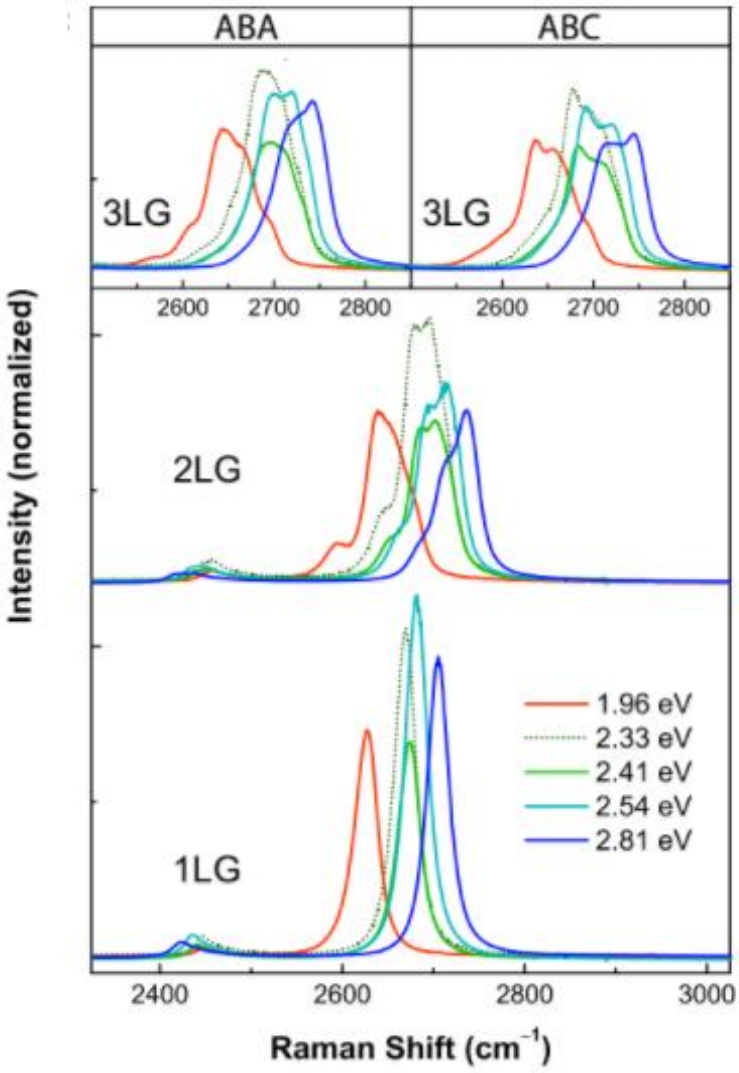

Figure 2.9 2TO(K) band of few-layers graphene with 2 different stacking orders under 5 different excitation energies. The intensity is normalized to the E_{2g} band intensity for each spectrum. (Adapted from [24]).

4) There are three process that make the factors in (2.1) vanish. One from the excitation, another from its emission, and from the phonons.

The electronic band of graphene, in accordance with section 2.2.2, evolves with the number of layers. In fact, a further distinction for the trilayer was made in [25], due to different stacking orders; ABA (Bernal stacking) and ABC (rhombohedral stacking). A dissimilarity on the Raman spectrum of graphene was reported in [24] due to this change in electron bands. The shape of the band is seen in Figure 2.9 while increasing the number of layers, and the distinction of the band for each stacking order in the trilayer graphene is also shown.

Disorder induced bands

The effect of breaking translational symmetry modifies momentum conservation rules, i.e., the fundamental rule for 1-phonon process. Lattice distortions from disorder could also lead to breakdown of other symmetry-based selection rules, activating $\boldsymbol{q} = 0$ phonons that are forbidden by symmetry of the unperturbed crystal structure. Generally, the effect of disorder of crystalline materials is a broadening of the Raman-allowed peak, the observation of new features related to symmetry forbidden scattering processes and, when the disorder is high, the phonon-density-of-states like spectra is observed.

When graphene is bombarded by a dose of ions, point defects are formed and the Raman spectra of this disordered structure exhibit two new features at ~1345 cm^{-1} and ~1625 cm^{-1}. Those new features have been called D and D' bands, respectively, from disorder. If we continue to use the notation proposed for the bands, those band will be called TO(K) and LO(Γ), respetively[5]. These bands are also dispersive. The sharpness depends on the quantity of disorder of the sample.

The processes for these bands are shown in Figure 2.10. The TO(K) band correspond to intervalley scattering, and the LO(Γ) band to intravalley scattering. Intravalley scattering means that the processes connect two points belonging to the same states around K. This distinction of scattering is important because at the edges of the sample, which can be viewed as extended defects (it break translational symmetry), the LO(Γ) band can still occur due to the that phonon/defect vectors occur in the same valley. The symmetry of those borders depends whether the TO(K) band is activated or not [23].

5) Even though this is a 1-phonon process, a defect acts as the second phonon. If the density of defects is not high, their effect on the wave functions can be treated perturbatively. This mean introducing more intermediate states in (2.1) as $\langle s_n | \hat{H}_{defect} | s_{n-1} \rangle$.

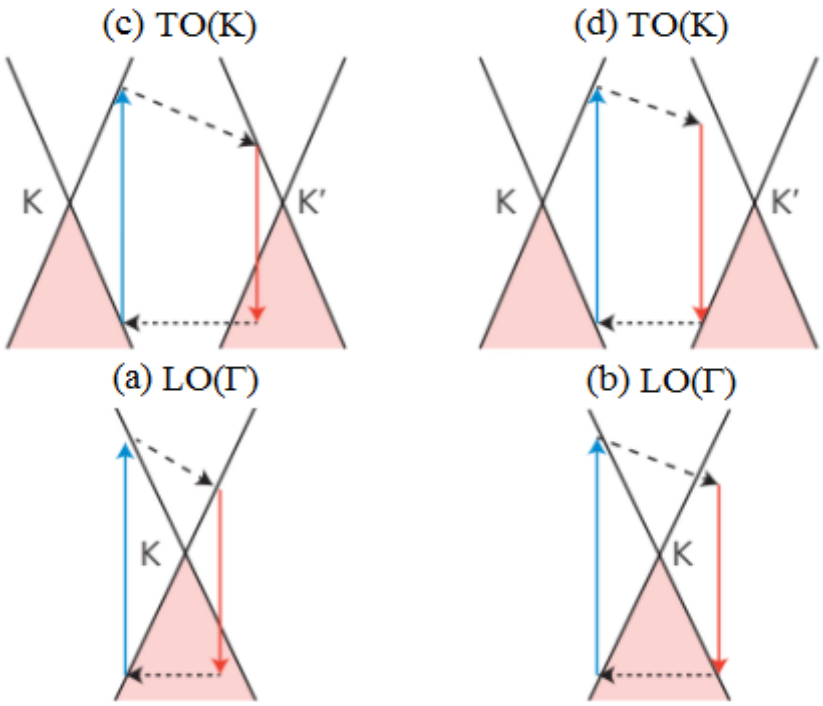

Figure 2.10 Raman processes for the TO(K) band **(a, b)** and LO(Γ) band **(c, d)**. Double resonance condition is displayed in all processes. Blue lines denote excitation, red line denote photon emission, and doted lines represent the wave vector of a phonon with certain energy. The defects are displayed as horizontal doted lines. (Adapted from [23]).

Other higher order bands

In addition to the 1-phonon defect-assisted process which gives rise to the TO(K) and LO(Γ) bands, a two-phonon defect-assisted processes can occur. This cause the so-called TO(K)+LA(K) band (~2450 cm^{-1}), making it a combination band. Furthermore, a two-phonon defect-free process leads to the 2LO(Γ) band (~3250 cm^{-1}), which is an overtone of the LO(Γ) band. These processes are shown in Figure 2.11. The combination band is due to intervalley scattering (Figure 2.11a) and the overtone band is due to intravalley scattering.

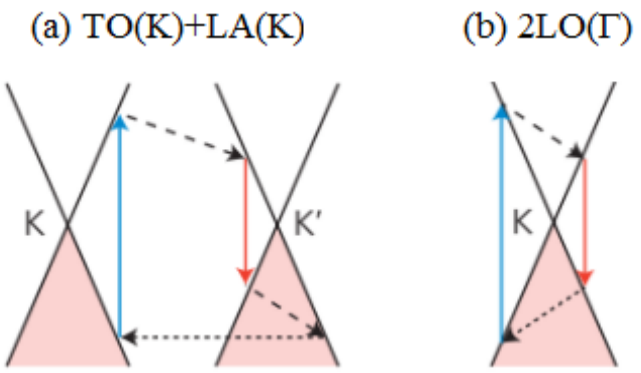

Figure 2.11 Raman processes for the TO(K)+LA(K) band **(a)** and 2LO(Γ) band **(b)**. Double resonance condition is displayed in all processes. Blue lines denote excitation, red line denote photon emission, and doted lines represent the wave vector of a phonon with certain energy. The defects are displayed as horizontal doted lines. (Adapted from [23]).

2.3. Raman spectroscopy of 2D TMDCs

2.3.1. Crystal structure of 2D TMDCs

The family of 2D TMDCs is composed of two adjacent sheets of chalcogen atoms that are separated by a sheet of transition metal atoms in a X-M-X configuration, making the monolayer an atomic trilayer structure. The intralayer M-X bonds are predominantly covalent in nature. The difference in the stacking order gives rise to different polytypes. For the semiconductor family used in this thesis (M = Mo, W and X= S, Se), the polytype under study is the trigonal prismatic (1H or AbA coordination, where upper cases represents the chalcogen atoms and lower cases represents the metal atoms), as shown in Figure 2.12a.

The unit cell of single layer MX_2 consists of three atoms, one metal atom M and two chalcogenide atoms X as seen in Figure 2.12b. Its primitive lattice vectors (see Figure 2.12c) are given by

$$\boldsymbol{a_1} = a\left(\frac{\sqrt{3}}{2}, \frac{1}{2}, 0\right) \qquad \boldsymbol{a_2} = a\left(\frac{\sqrt{3}}{2}, -\frac{1}{2}, 0\right), \tag{2.11}$$

where the a value is around 0.316 nm and 0.33 nm, depending on the material. Likewise, the reciprocal lattice vectors are written as

$$\boldsymbol{b_1} = \frac{2\pi}{a}\left(\frac{\sqrt{3}}{3}, 1{,}0\right) \qquad \boldsymbol{b_2} = \frac{2\pi}{a}\left(-\frac{\sqrt{3}}{3}, 1{,}0\right). \tag{2.12}$$

The high symmetry points of the Brillouin zone are displayed in Figure 2.12d. It has the same reciprocal lattice and high symmetry points as in graphene.

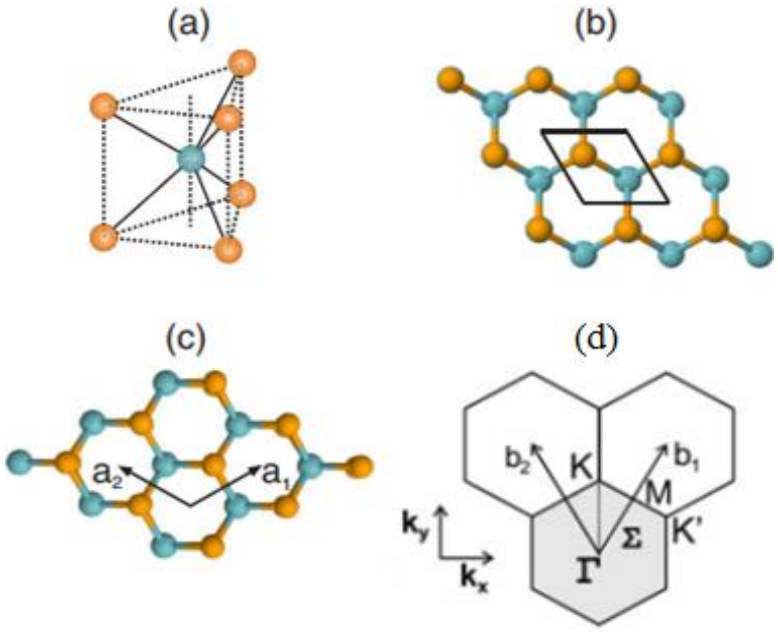

Figure 2.12 (a) Transition metal atom coordination for trigonal prismatic polytype. The blue spheres represent transition metal atoms and orange ones, chalcogen atoms. **(b)** Top view of 2D TMDCs with its unit cell marked in the black rhombus. **(c)** Top view of 2D TMDCs with its primitive unit vectors. (Adapted from [25]).

When the number of layers is odd or even, the space group of the wave vectors at each high-symmetry point or line is defined with different symmetries. The group is like the one found for *N*-layers graphene, however, the monolayer case of TMDCs lacks inversion symmetry, and therefore belongs to the same space as that for other *N*-odd layers. Table 2.2 shows the group of the wave vector for different high symmetry points and lines within the Brillouin zone.

Table 2.2 The space group and the group of the wave vector for *N*-layer TMDCs and bulk TMDCs at all high symmetry points. (Adapted from [25]).

	Space group	**Γ**	**K(K')**	**M**	**T(T')**	**Σ**	**u**
N odd	$P\bar{6}m2$	D_{3h}^{1}	C_{3h}^{1}	C_{2v}^{14}	C_{s}^{1}	C_{2v}^{14}	C_{1}^{1}
N even	$P\bar{3}m1$	D_{3d}^{3}	D_{3}^{2}	C_{2h}^{3}	C_{2}^{3}	C_{s}^{3}	C_{1}^{1}
N infinite	$P6_3/mmc$	D_{6h}^{4}	D_{3h}^{4}	D_{2h}^{17}	C_{2v}^{16}	C_{2v}^{14}	C_{s}^{1}

2.3.2. Electrons in 2D TMDCs

The electron energy dispersion of monolayer and few-layers TMDCs has been investigated both experimentally and using first-principles calculations. The most interesting property of 2D TMDCs is its strong photoluminescence (PL) due to its direct-band gap in the monolayer (1L-MX_2) [26]. This bandgap opening from its bulk counterpart is associated with quantum confinement [27].

For TMDCs, the atoms are heavy, and the outer electrons states are d orbitals that have a strong spin-orbit coupling (SOC). This coupling removes the degeneracy in both the conduction and valence band, making an energy splitting between spin up and spin down states. Table 2.3 shows the theoretical energy of the spin-orbit coupling.

Table 2.3 Theoretical energy of the spin-orbit coupling of MoS_2, $MoSe_2$, WS_2, and WSe_2. (Adapted from [28] and [29])

MX_2	Valence band splitting (eV)	Conduction band splitting (eV)
MoS_2	0.148	0.003
WS_2	0.430	0.026
$MoSe_2$	0.184	0.007
WSe_2	0.466	0.038

Contrary to what happens in graphene, the valence and conduction bands of 2D TMDCs present a very rich orbital contribution (see Figure 2.13). Electronic states near the conduction band (CB) minimum and valence band (VB) maximum contributed mainly from *d* orbitals (yellow) of the M atom and the *p* orbitals (green) of the X atom.

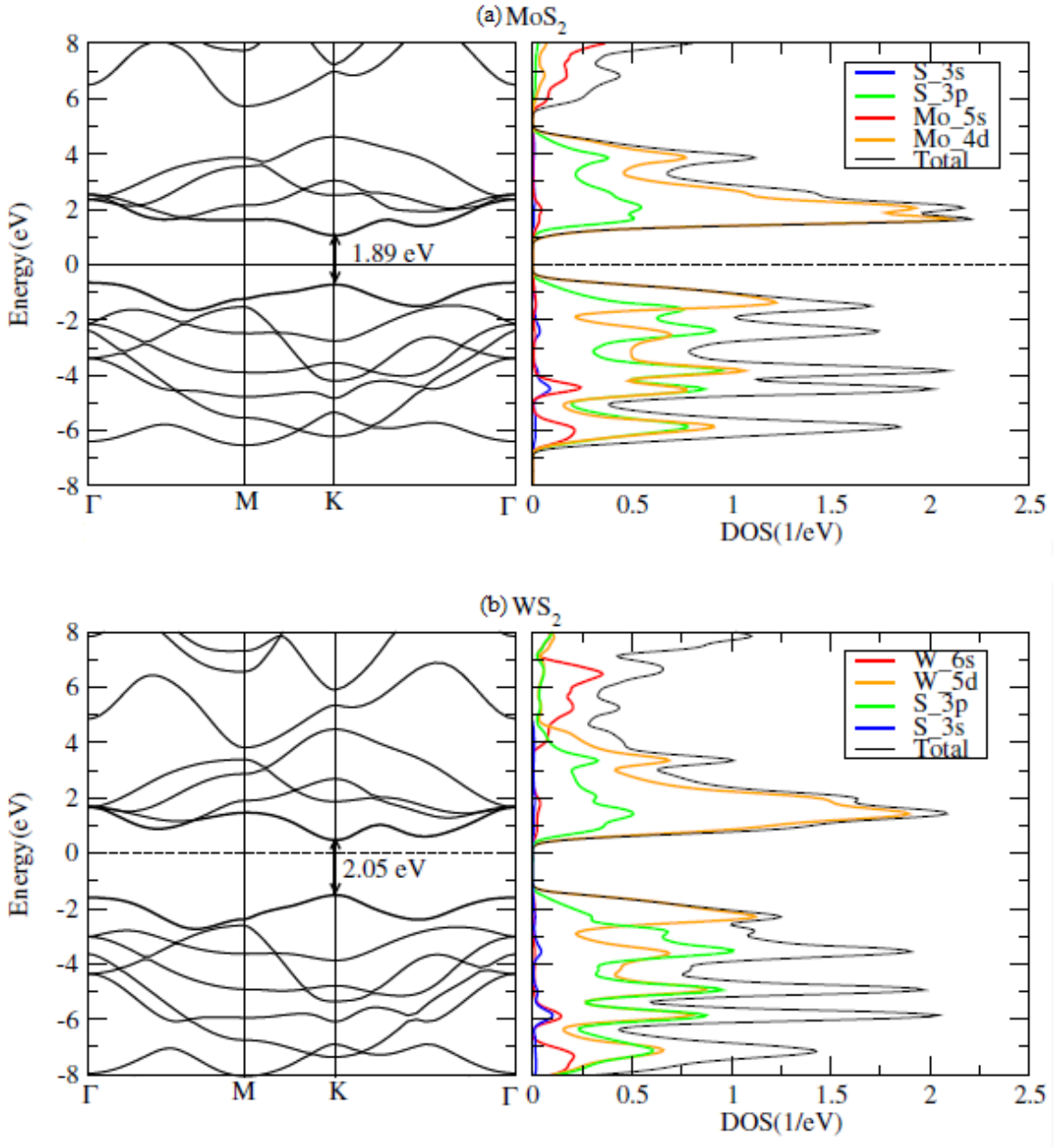

Figure 2.13 Electronic band structure without SOC of **(a)** MoS_2 and **(b)** WS_2 with its density of states. The energy of the band gap is displayed in both cases. (Adapted from [30]).

In the monolayers of TMDCs, the CB maximum and VB minimum are both located in the corners of the first Brillouin zone, which correspond to the K(K') points. The CB also has a local minimum at the low symmetry Q point (between Γ and K), while the VB has a local maximum at the Γ point. These points are close in energy to the CB maximum and VB minimum around K. In certain cases, these local extrema may become global extrema [27].

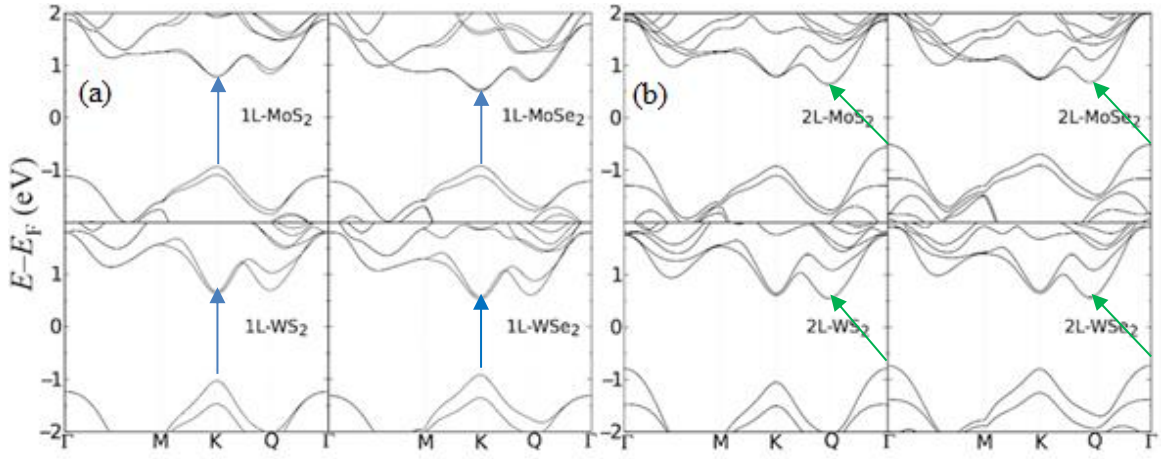

Figure 2.14 Electronic band structure with SOC of **(a)** monolayer, and **(b)** bilayer MoS_2, $MoSe_2$, WS_2, and WSe_2. Direct to indirect transition is displayed. (Adapted from [27]).

For bilayers of TMDCs, in the case of MoS_2, $MoSe_2$, WS_2, and WSe_2, the stacking symmetry is called 2Hc (/CaC AcA/ stacking) [31]. The direct bandgap to indirect bandgap transformation (see Figure 2.14) is consequence of the interlayer interaction [27]. The splitting of points Γ and Q in the valence band are notably larger than at the K point of the VB. At the same time, at the K point of the CB, there is no visible splitting from the interlayer interaction. This is due to the 2Hc symmetry of the bilayer lattice [27].

2.3.3. Phonons in 2D TMDCs

The phonon dispersion of monolayer MX_2 (1L-MX_2) has three acoustic and six optical branches inherited from the nine vibrational modes at the Γ point. The three acoustic branches are the in-plane longitudinal acoustic (LA), the transverse acoustic (TA), and the out-of-plane acoustic (ZA) modes. The six optical branches are two in-plane longitudinal optical (LO_1 and LO_2), two in-plane transverse optical (TO_1 and TO_2), and two out-of-plane optical (ZO_1 and ZO_2) branches. The same features are observed for each material of the TMDs as seen Figure 2.15 and Figure 2.16. Each phonon band are shifted in frequency because of difference in mass of the atoms used [32].

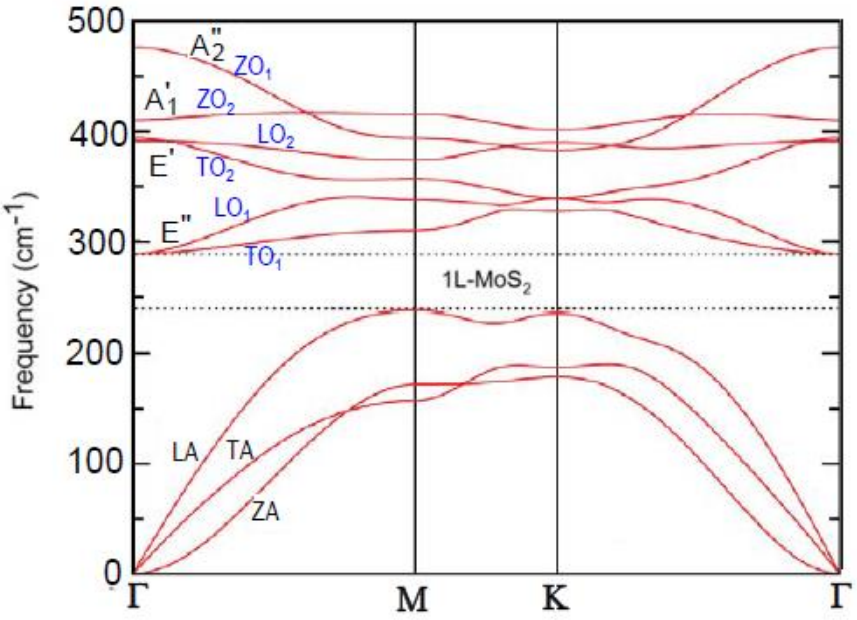

Figure 2.15 Phonon for 1L-MoS_2 showing the optical and acoustic branches. (Adapted from [32]).

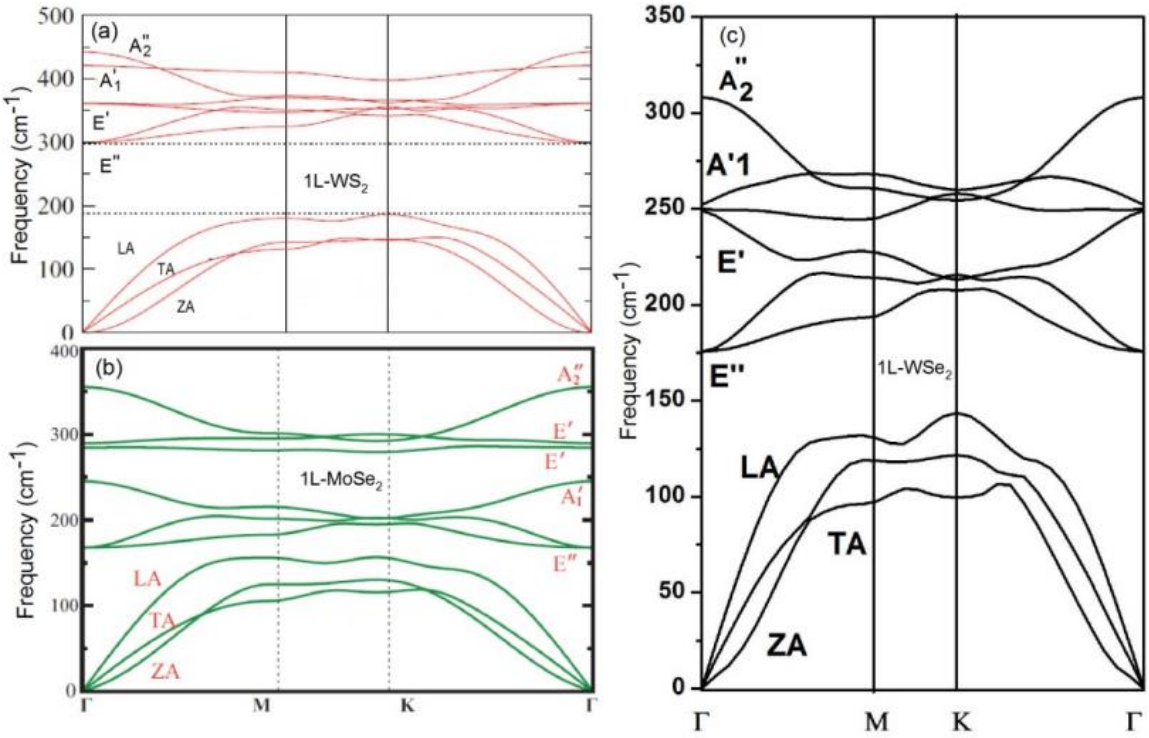

Figure 2.16 Phonon dispersions for **(a)** 1L-WS_2, **(b)** 1L-$MoSe_2$ and **(c)** 1L-WSe_2. (Adapted from [32]).

The vibrational modes responsible for the non-translational of the crystal modes are represented in Figure 2.17. The Raman-active modes for first-order Raman scattering in TMDCs also depends on the number of layers since the high-symmetry Γ point have different group of wave vector. Those modes are:

$$\Gamma^{Raman} = \frac{(3N-1)}{2}(E' + E'' + A'_1), \text{ for } N \text{ odd},$$
$$\Gamma^{Raman} = \frac{3N}{2}(E_g + A_{1g}), \text{ for } N \text{ even}. \quad (2.13)$$

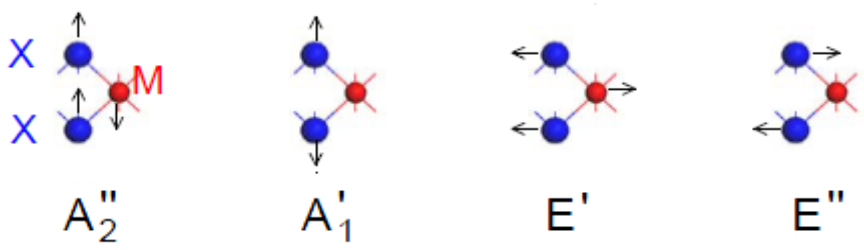

Figure 2.17 Graphic representation of the atomic motion of the metal (M) and chalcogens (X) atoms for each mode. (Adapted from [32]).

2.3.4. Main bands in Raman spectra of 2D TMDCs

Following the notation mentioned in 2.2.4, we will call the first-order bands (1-phonon process) by the modes in the Γ point. Higher-order will be called by the contribution of the phonon branches around a specific point. These multiphonon processes will be relatively weak compared to the first-order bands if the process is not resonant. To be resonant, the excitation energy must match the gap between the VB and CB. This gap lies between 1.52-2.28 eV, depending on the material. Because of this dependence of the excitation energy, the Raman spectroscopy of 2D TMDCs is not well established as in graphene. We will, however, review the existing results.

A'_1 and E' band

These band follows the normal notation of its point group. In most literatures, although the point group notation changes with the number of layers, the same notation for the monolayer is used. In fact, early studies of Raman spectroscopy of 2D TMDCs, the point group of the

bulk TMDCs was used to name this band. These band are related to the out-of-plane (A_1' band) and in-plane (E' band) motion of the atoms.

Main findings on both bands was that the E' mode is red shifted, and the A_1' mode is blue shifted with increasing the number of layers. This makes the vibration softened and stiffened, respectively. The difference in the position and intensities of both peaks in the Raman spectrum was proposed as an efficient method to identify the thickness of the material. Moreover, the intensity of these bands depends on the energy used as excitation, because unlike graphene, not all photon energies used are resonant.

Disorder induced bands

As well as in graphene, one might expect new features in the Raman spectrum of 2D TMDCs upon creating disorder in the sample by any mean (bombardment of ions, for example). It was reported many years ago that disorder-induced Raman bands also appear in the spectrum of MoS_2 and WS_2 films [33]. Recent studies have also observed these new features in form of additional peaks [34].

These bands involve phonons of other branches within the interior of the Brillouin zone and their frequencies correspond to the frequencies of the phonon of the LA branch at the M or K point. Therefore, we call this disorder-induced feature as the LA(M/K) band. Both notations are used depending on the author, meaning that this band has been not well established.

Other higher order bands

A detailed study of higher order bands in 2D TMDCs can be found for MoS_2, WS_2, and WSe_2 in [32] and in [36] for $MoSe_2$. Here we will focus on the most intense second-order band, which involves a 2-phonon process of the LA branch with opposite wavevector, making it possible to meet the fundamental selection rule of Raman scattering. This band is called the 2LA(M/K) band. Intriguingly, this band does not have a dispersion behavior like the G' band in graphene with the excitation source but for certain energies, its intensity is higher than the first-order bands (see Figure 2.18 for the case of MoS_2).

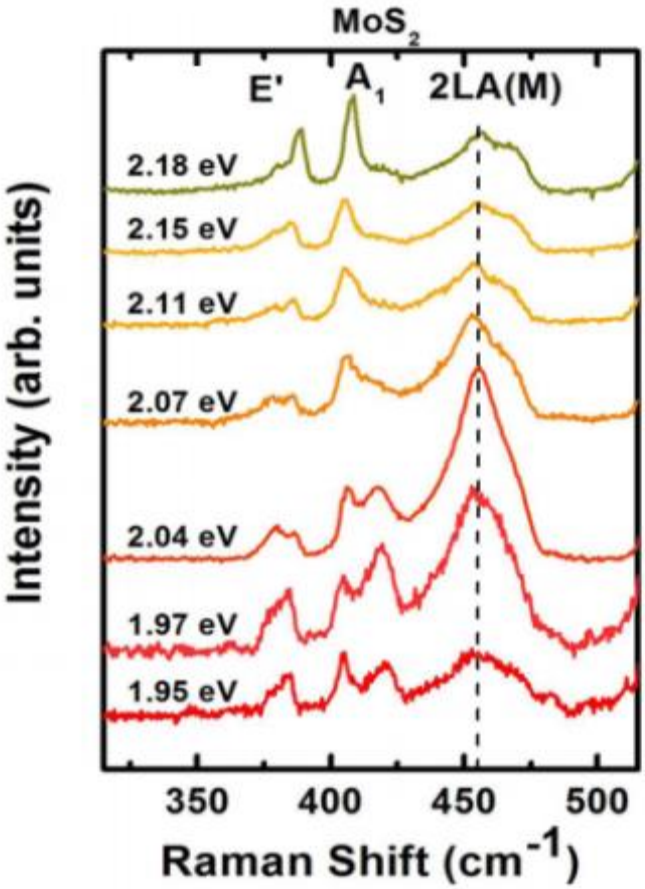

Figure 2.18 Dependence of the bands of MoS_2 on the laser energies. The 2LA band was assigned for the M point in this case. (Adapted from [22]).

Over the years, nonetheless, Raman spectroscopy techniques have been improved, making possible to obtain a better resolution of the Raman spectra. In recent work [34], it was demonstrated that the 2LA(M/K) band was composed by several peaks in the case of monolayer. The assignation of higher-order bands in 2D TMDCs are still lacking because different authors use different assignations. Double resonance mechanisms have been proposed to explain this [22].

3. Methodology

In this chapter, the methods used to study of the scattered radiation explained in chapter 2 will be reviewed. The preparation of the samples will be explained as well as the setup used for the manipulation of the incident and scattered light. The results obtained using this approach will be presented in the next chapter.

3.1. Sample

The most common approach to exfoliate graphene from graphite is the scotch tape method (see Figure 3.1). Initially, commercial highly ordered pyrolytic graphite (2SPI supplies) and TMDCs crystals (2D Semiconductors) are separated in single to few-layers by means of micromechanical cleavage. - Because the surface energy of TMDCs (65-120 mJ/m^2 [35]) are similar to the surface energy of graphene (65-120 mJ/m^2 [36]), it makes them possible to cleavage in the same approach.

Single layer graphene absorbs only 2.3% of the visible light. This make difficult to identify areas of single- or few-layers graphene. However, it was show that if silicon with appropriate oxide thickness is used as substrate, the contrast is increased by means of interference effects [37]. With this, is possible to making it visible by eye using an optical microscope. This fact allows a rapid identification of layers. A higher contrast is observed for TMDCs with certain thickness of oxide [38], since a single layer of TMDCs can absorb up to 20% of light [39].

Commercial Si wafers with an SiO_2 thick around 290 nm (for graphene) and 90 nm (for TMDCs) were cut in small squares of around 10 mm, which were used for substrate. This substrate was previously cleaned with ultrasonic cleaning and plasma cleaning equipment. Baths of acetone, isopropyl alcohol, and water were used in the ultrasonic cleaning (~50 kHz) for 5 minutes each. As for the plasma cleaning, the substrates were placed in vacuum chamber that was later injected with O_2 at 2 atm. Microwave radiation were used to spark the plasma of the chamber for 30 seconds.

After the substrate is thoroughly cleaned, the exfoliated crystals were deposited as follows; sticky side of scotch tape is placed on the bulk crystal (Figure 3.1a), then it is removed from the crystal and layers of material are stuck in the tape (Figure 3.1b). The sticky side of the tape with the material is placed on a substrate (Figure 3.1c) and it is baked at 100 °C for 2 minutes at 1 atm. The tape is removed, in a fast move, leaving layers on the substrate (Figure 3.1d). Residues of the tape can be seen on the sample.

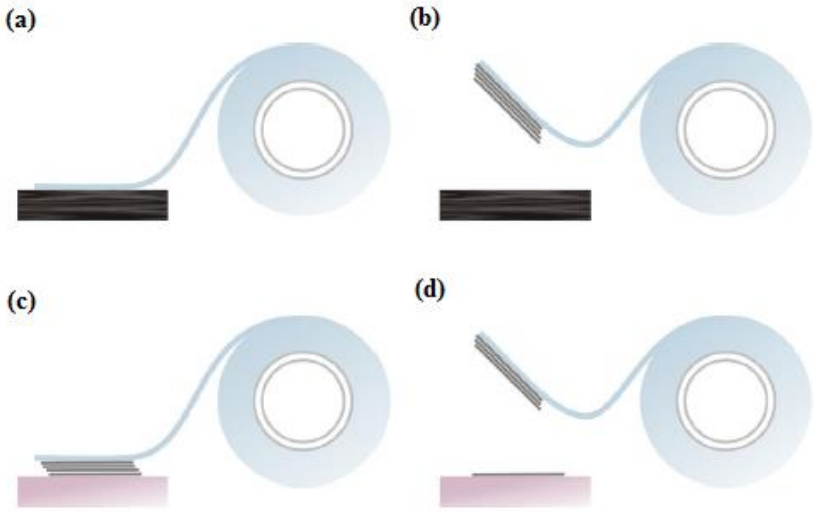

Figure 3.1 Scotch tape method. (Adapted from [1]).

In order to localize the few-layers of material, the sample is illuminated by a halogen lamp (Model ACE from SCHOTT) with a flexible optic fiber (model A08026 from SCHOTT). The image is displayed in PC1 with help of the software NOVA NT-MDT with a camera (model STC-MC83USB from SENTECH). An objective of 10x is initially used for a faster localization of a possible zone of interest (Figure 3.2a), then an objective of 100x is used to verify if this zone has few-layers of material (Figure 3.2b). The sample is placed on a *xy* manual positioner (model NTEGRA Spectra II from NT-MDT).

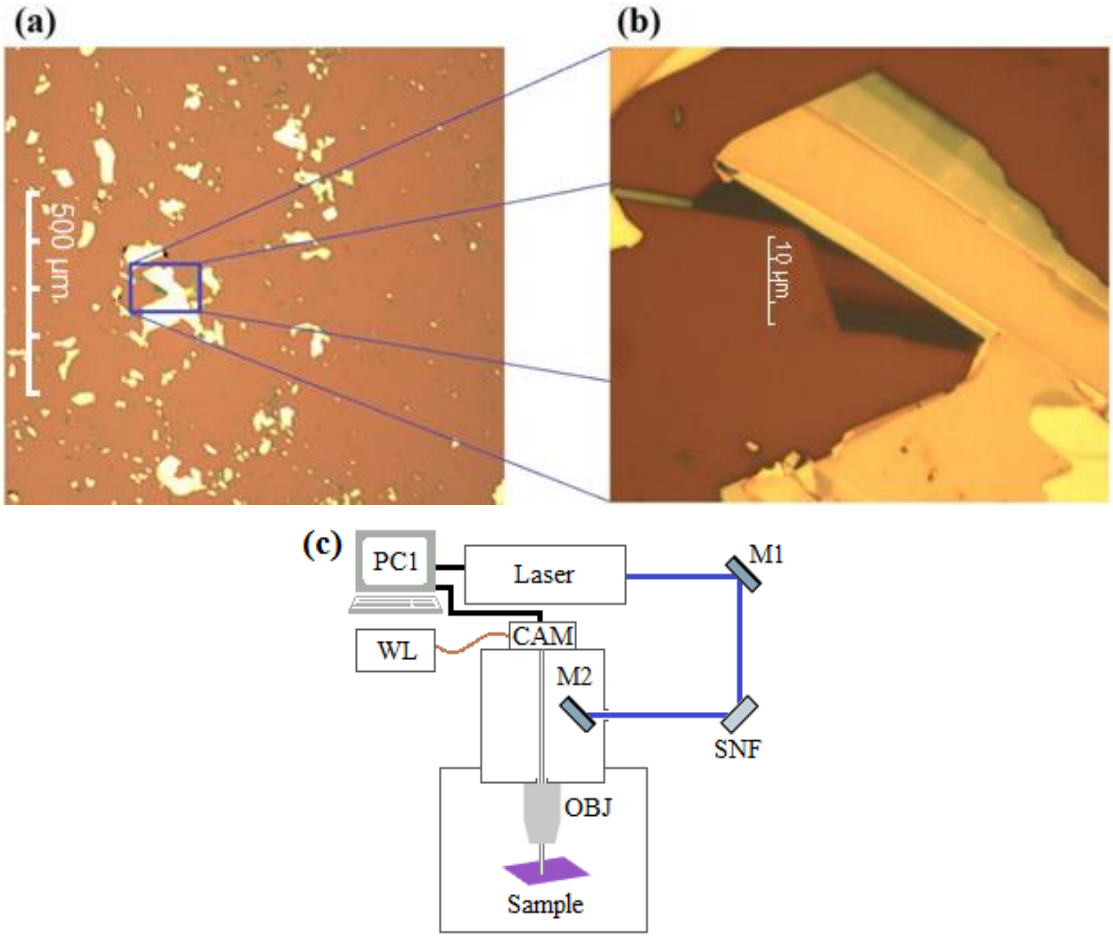

Figure 3.2 Image of the sample with an objective of 10x **(a)** and 100x **(b)**. The setup for capturing the image also shown **(c)**.

To see the sample, the white light (WL) goes through the optic fiber (brown line) and the objective (OBJ) to illuminate the sample. The light reflects to the camera (CAM), which is in the same line of the white light (see Figure 3.2c) and captures the image in PC1. **Note that if the laser is on**, it hits the first mirror (M1), then on the single-notch filer (SNF), which for now we consider it a mirror, and finally in the back of the second mirror (M2).

The mirror M2 can be moved in two configurations: to allow the laser to hit the sample or to allow the white light to hit the sample, then the camera. In the second case, the mirror transmits a small fraction of the laser intensity which reaches the camera and allows to precisely locate the excitation position over the sample. In this work, we were able to localize two zones with few-layers made from the highly ordered pyrolytic graphite and six

zones made from the TMDCs crystals, as seen in Table 3.1. The details of the laser and single-notch filter are in the next section.

Table 3.1 Zones of interest for graphene and TMDCs. The images were captured with an objective 100x. The scales are shown for each image.

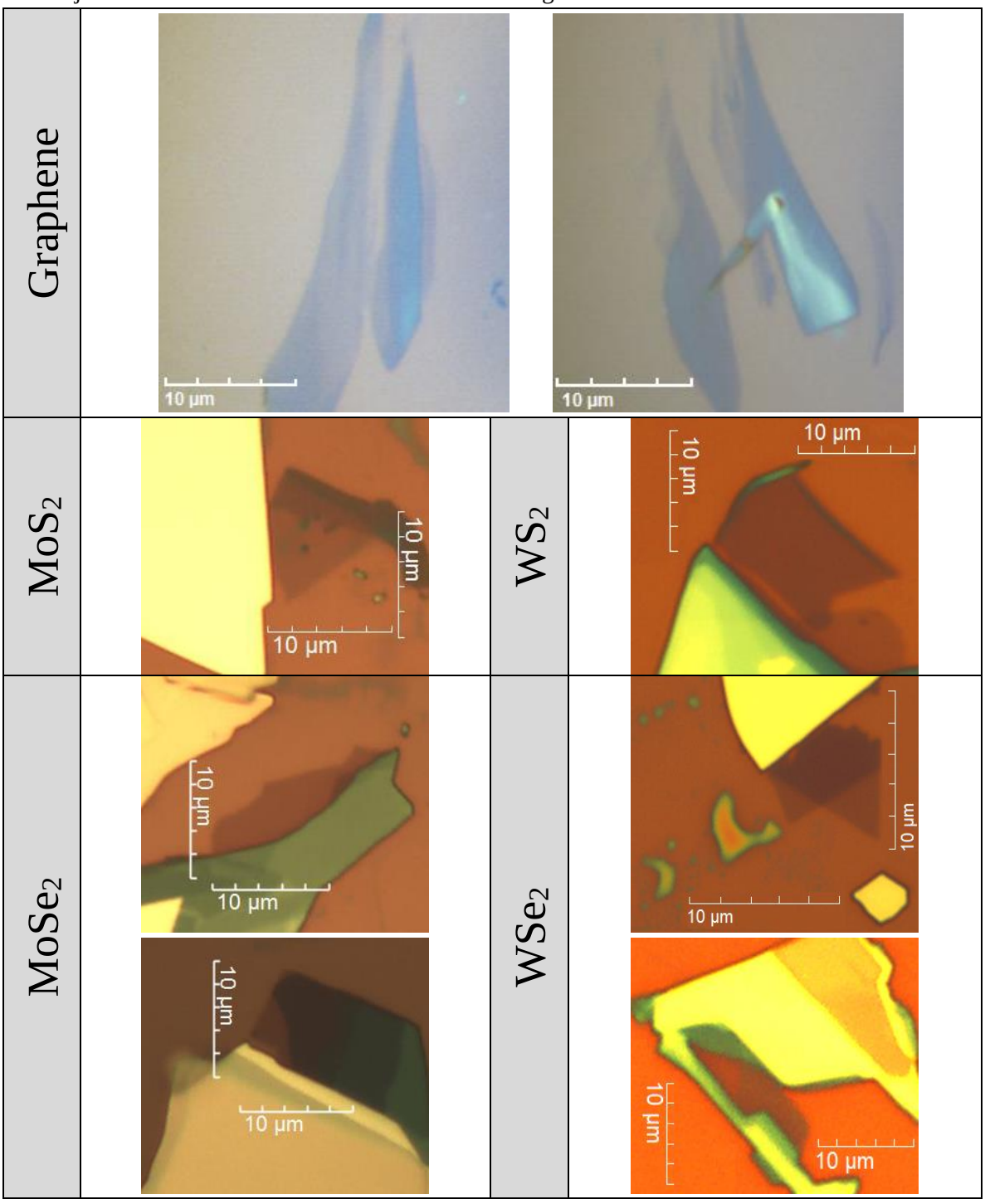

3.2. Raman microspectroscopy

The setup is just an optical Raman setup coupled with and objective and a *xy* manual positioner which acts as a microscope. As mentioned above, the mirror M2 is moved to allow the laser to hit the sample. The laser (blue line) hits the mirror M1, then the SNF (which acts as a mirror). The reflected light from the SNF hits the mirror M2 and enters the objective (100x with 0.9 *NA*) to hit the sample. The diameter *d* of the laser spot can be estimated with the wavelength used and the objective Numeric Aperture (NA) from $d = 1.22\lambda/NA$, where *d* is the diameter of the spot. The reflected light goes to the mirror M2, which allows 0.1% of light to be transmitted making possible to see the laser spot on the camera.

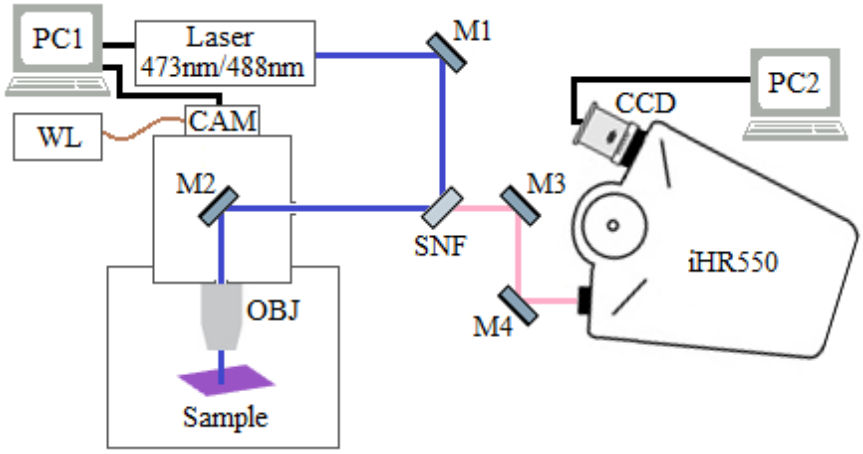

Figure 3.3 Raman microscopy setup. M stand for mirror, SNF for single-notch filter, and OBJ for objective.

For graphene, a laser of wavelength 473 nm (Model Excelsion One 473 from SPECTRA-PHYSICS) was used and for TMDCS a laser of wavelength 488 nm (Model OBIS 488LS-20 from COHERENT). Two different single-notch filters, one for each laser, were used (model NF03-488E and NF03-473E from Semrock). The power of those lasers are controlled by PC1. Following the reflection from the sample to the mirror M2, the laser-signal beam hits the SNF which decrease the transmitted laser intensity around six orders of magnitude within a 14 nm bandwidth around the laser line. The rest of the light that was shifted due to Raman scattering (pink line) is transmitted without significant loss (~5%). This light is collected in a Synapse Back-Illuminated Deep-Depletion 1024 × 256 Charge Coupled

Device (CCD) from HORIBA with help of a spectrometer (iHR550) with a monochromator with a grating of 1200 lines/mm controlled bythe software LabSpec6 (PC2). The CCD needs to operate at -70 °C, which can be controlled with PC2. The monochromator diffracts the light depending on the wavelength, thus, we can identify different scattered light. The spectral response of the detector in the visible region has around 90% of quantum efficiency.

3.3. Data analysis

Raman spectrum of a sample were acquired at a single point with spots around 0.64 μm (laser 473 nm) and around 0.66 μm (laser 488 nm) where the scattering event occur. For this dissertation, we acquired data with an acquisition time of 10-20 seconds with 10-20 repetitions to smooth the curve obtained. This make 100-400 seconds to obtain a single point. The typical Raman plot (Figure 3.4b), would have the energy shift from the excitation on horizontal axis, called Raman shift. The intensity of the plot, is only affected by the time of acquisition, therefore we can use arbitrary units (a. u.) for the vertical axis.

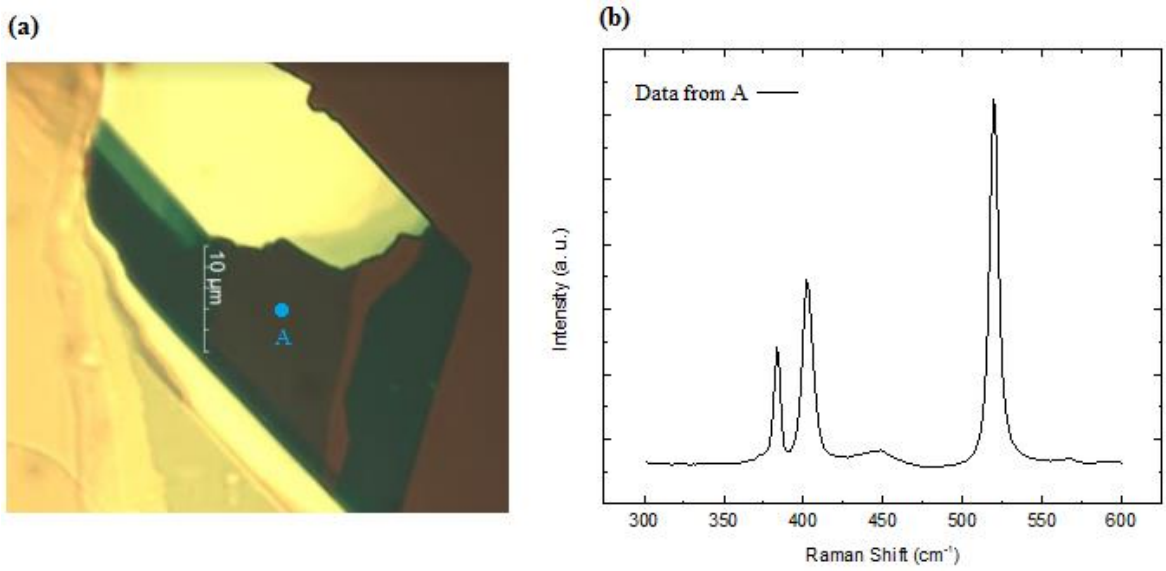

Figure 3.4 (a) Optical image of MoS_2 under a 100x objective, where the blue point indicates the focus of the laser spot. **(b)** Raman plot obtained from the point A.

To make a correction of the experimental data, a measurement of the substrate (Si) band is made and its calibrated to coincide with 520 cm^{-1}. The intensity does not need correction (normalization), because the Raman peaks are narrow, and the corresponding spectral range is short. Small spikes appear in the spectrum due to cosmic rays, which can be eliminated from the data.

Regarding the analysis of the spectra, phonon excitations can be approximated as a Lorentzian profile [40]. When a feature is composed of several phonon contributions, the shape is determined by a convolution of different Lorentzian curves. Additional broadening factors exists, like thermal broadening and by instrumental resolution, which we will describe with a Gaussian profile. When combining both Lorentzian and Gaussian, the resulting profile is known as Voigt profile. In the analysis, we used the Voigt profile for high intensity peak in TMDCs, and Lorentzian for the rest. In graphene, it is well stablished the use of Lorentzian for all bands [19].

To fit the profiles, we used OriginPro 9 (OriginLab Corporation). To adjust the curves, we first selected the maxima of the most prominent bands with its corresponding profile. After that, small bands contributions were analyzed adding bands one by one. For example, for Lorentzian profile, it is adjusted to the function:

$$I(\omega) = I_0 + \frac{2A}{\pi}\left(\frac{\omega_w}{4(\omega - \omega_c)^2 + \omega_w^2}\right), \tag{3.1}$$

where I_0 is the initial offset of intensity, A the area of the fitted curve, ω_c the center of the curve, and ω_w its full width at half maximum. Constrictions and fixed parameters can be used to reduce the number of iterations used to calculate.

The goodness of fit was tested with the fitting deviation (or residual) which plots the difference between the observed value and the predicted value. The coefficient of determination (R^2) was also used. This is the proportion of the variance in the dependent variable that is predictable from the independent variable. A $R^2 = 0.5$ implies that 50% of the variability between the two variables has been accounted for, and the remaining 50% of the variability is still unaccounted for.

4. Experimental results

In this chapter, it is presented the Raman spectrum of graphene (473 nm excitation) and TMDCs (488 nm excitation). The five following sections reviews the results of few-layers graphene, few-layers MoS_2, few-layers WS_2, few-layers $MoSe_2$, and few-layers WSe_2. A deconvolution of each spectrum is made, and its parameters are listed in Appendix A and B.

4.1. Few-layers graphene

For the system of few-layers graphene, the Raman spectrum is displayed in Figure 4.1. The measured points, called T1, T2, T3, and T4 are distinguish. The most prominent Raman features are the E_{2g} band around 1580 cm^{-1} and the 2TO(K) band around 2700 cm^{-1}. Small bands are also appreciable as the TO(K)+LA(K) band around 2450 cm^{-1} and the 2LO(Γ) band around 3250 cm^{-1}. An analysis of the spectra is used to determine the number of layers and its stacking configuration.

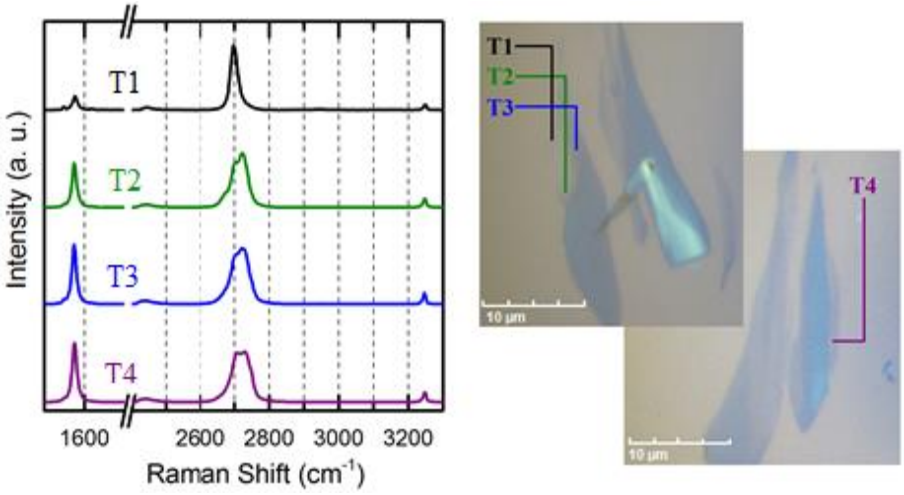

Figure 4.1 Raman spectrum of few-layers graphene of the points T1, T2, T3 and T4.

A relation between intensities of the bands E_{2g} and 2TO(K) can be used to have a first evidence of the number of layers. It was reported in [41] that the ratio $I(E_{2g})/I(2TO(K))$ was roughly 0.2 and 0.8 for monolayer and bilayer graphene on Si/SiO_2 substrates. However, the lineshape of the 2TO(K) band gives a better way of determining not just the number of layers, but also, its stacking configuration. Figure 4.2 shows the deconvolution of the E_{2g} and 2TO(K) bands.

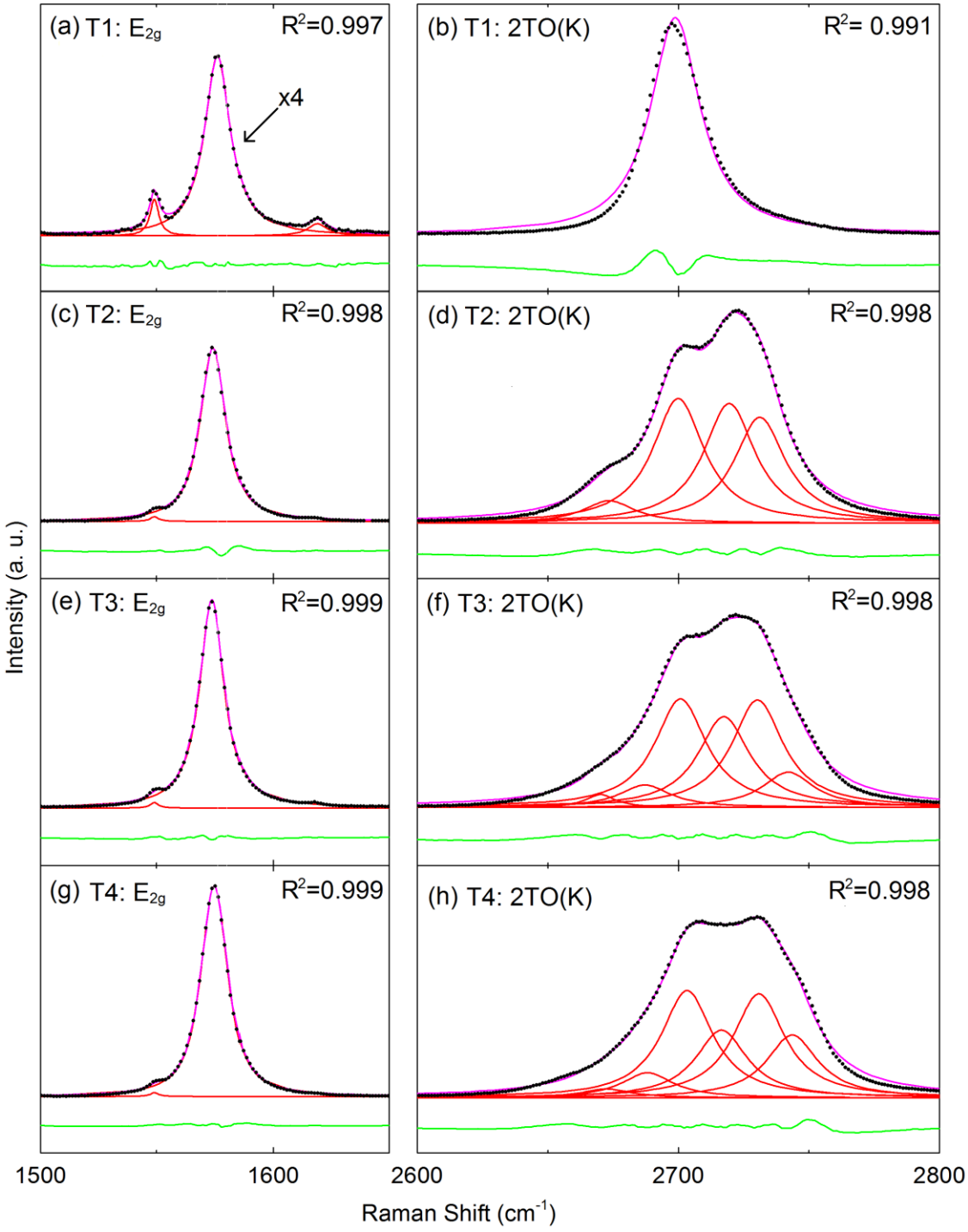

Figure 4.2 Fitted curves (red) with the data (black points) along with the residual (green) and its cumulative fitting curve (magenta) for the E2g and 2TO(K) bands at points: **(a, b)** T1, **(c, d)** T2, **(e, f)** T3, and **(g, h)** T4, in few-layers graphene. Coefficient of determination (R^2) is shown for each case.

The deconvolution of the E_{2g} band (Figure 4.2a) shows small peaks in the right side and left side of this band. The higher frequency peak is due the LO(Γ) band associated to disorder effects (explained below). The lower frequency peak appears in all measurements and we assume that is related to external factors, because its position and width, remained the same for all samples (see Appendix A). The E_{2g} band appears at 1576 cm^{-1}, which differs 6 cm^{-1} from that reported in [19]. This down-shift could be due to an increase in the temperature sample because the high laser power or the sample could be suspended [42].

In early studies of graphene, a symmetric 2TO(K) band on Si/SiO_2 substrates was identified as a signature of a single layer [19]. However, later studies showed that the intrinsic lineshape is asymmetric in suspended single layer graphene samples [43, 44]. In our results, the fitting in Figure 4.2b shows that the 2TO(K) band is asymmetric. Combining this evidence with the observed down-shift of the E_{2g} band, allows us to conclude that point T1 corresponds to a single layer graphene (1-LG) suspended by means of a thicker zone. The intensity ratio $I(E_{2g})/I(2TO(K)) = 0.2$ also corroborates that T1 is 1-LG.

Figure 4.2c and Figure 4.2d show the E_{2g} band and 2TO(K) band for point T2, respectively. Its intensity ratio $I(E_{2g})/I(2TO(K)) = 0.8$ gives a first evidence that corresponds to a bilayer graphene. The deconvolution of the 2TO(K) band requires four Lorentzian as was reported for a bilayer graphene [45]. Note that this band is dispersive (see section 2.2.4), meaning that comparation of results must be done with caution. The E_{2g} band in this case is also down-shifted by 5 cm^{-1}, perhaps by temperature changes or a nonintentional doping [42].

Figure 4.2f and 4.2h shows that it is required six Lorentzian to adjust the 2TO(K) band for the points T3 and T4, respectively. This confirms that those points correspond to trilayer graphene, as reported in [19]. However, the line shape for T3 and T4 are different. Comparing our results with that reported in [24], reproduced in Figure 2.9 above, and considering our excitation at around 2.62 eV (473 nm), we concluded that T3 corresponds to a trilayer graphene in the ABA stacking configuration, and T4 to a trilayer graphene in the ABC stacking configuration.

As mention above, the LO(Γ) band that appears in the lower frequency side of the E_{2g} band is related to disorder, specifically the edge of the exfoliated sample [23]. This can be confirmed in Figure 4.3, that shows the TO(K) band for the point T1. This band was not observed for the points T2, T3, and T4.

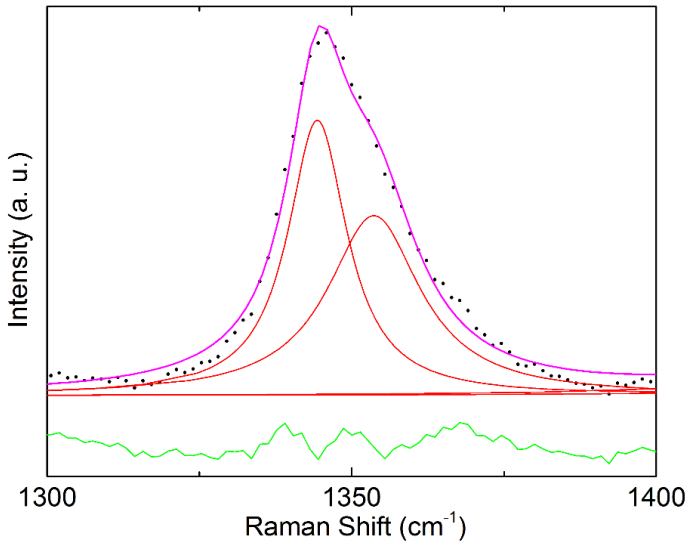

Figure 4.3 Fitted curves (red) with the data (black points) along with the residual (green) and its cumulative fitting curve o (magenta) for the TO(K) band at point T1.

Regarding the rest of the second-order band are presented in Figure 4.4. The TO(K)+LA(K) band was reported to be fitted with two Lorentzian curves for a single layer graphene [46]. We could not fit this band with two curves for the points T2, T3 and T4. We attempt to add more Lorentzian curves until the coefficient of determination (R^2) was close to 0.99, making four curves for bilayer (T2) and five curves for trilayer (T3 and T4).

A proper analysis of the 2LO(Γ) band has not been reported either, mentioned in [47], but not analyzed. Our results show that a single Lorentzian curve is enough to fit this band (Figure 4.4b, 4.4d, 4.4f, and 4.4h). The single band is explained since it originates from phonons around Γ, making a single contribution (**q** = 0). Our results also show that this band is down-shifted by increasing the number of layers and shows similar width in all cases.

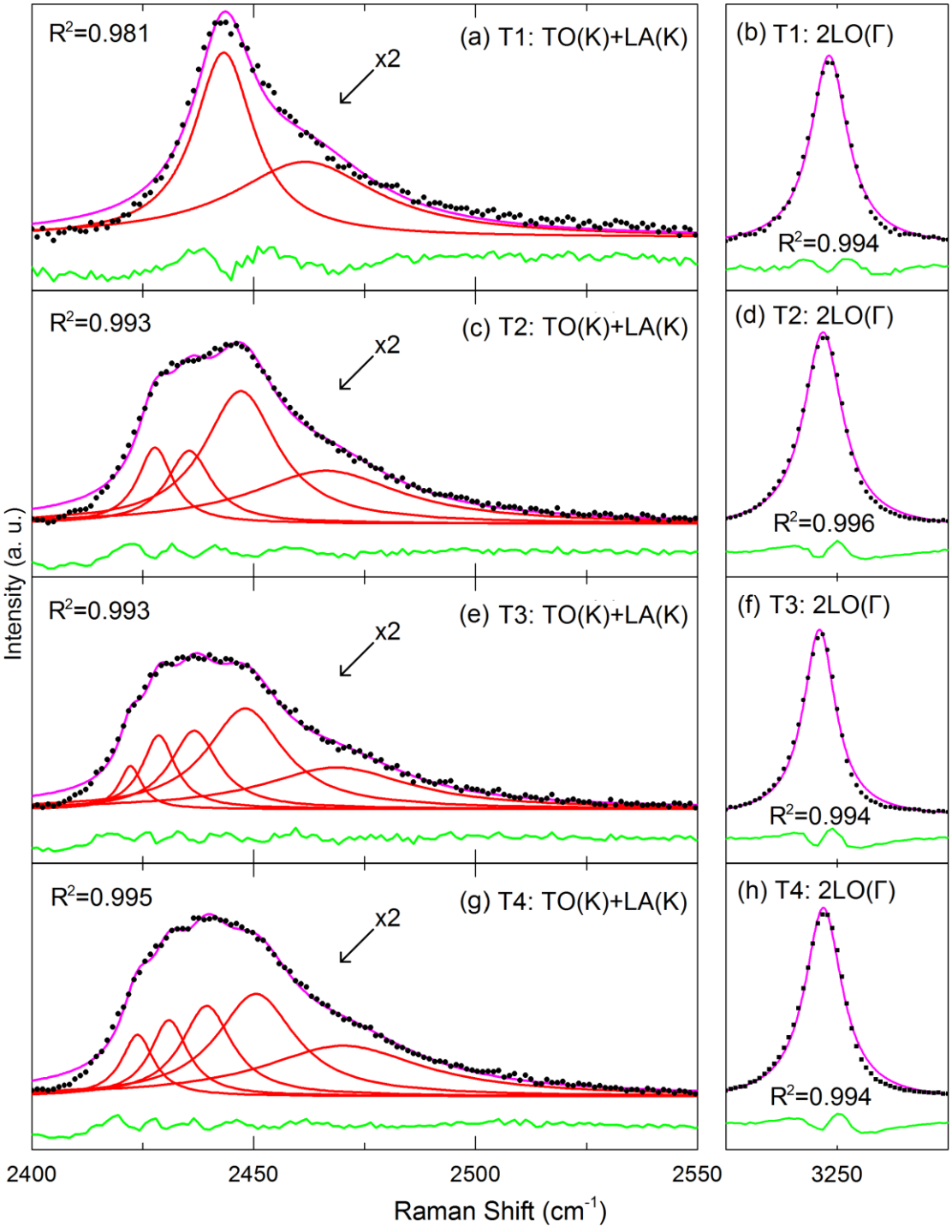

Figure 4.4 Fitted curves (red) with the data (black points) along with the residual (green) and its cumulative fitting curve o (magenta) for the TO(K)+LA(K) and 2LO(Γ) bands at points: **(a, b)** T1, **(c, d)** T2, **(e, f)** T3, and **(g, h)** T4, in few-layers graphene. Coefficient of determination (R^2) is shown for each case.

4.2. Few-layers molybdenum disulfide (MoS_2)

Figure 4.5 shows the Raman spectra of different samples of molybdenum disulfide (MoS_2). We observe only main contribution of the first-order peaks around 370-420 cm^{-1}. This is expected, since not all excitation energies are resonant, like graphene. To be resonant, the excitation needs to be close to the bandgap of the material (see Figures 2.14 and 2.18). In this region the E′ band related to the in-plane motion of the atoms (lower frequency side), and the A_1' band related to the out-of-plane motion of the atoms (higher frequency side), can be distinguish.

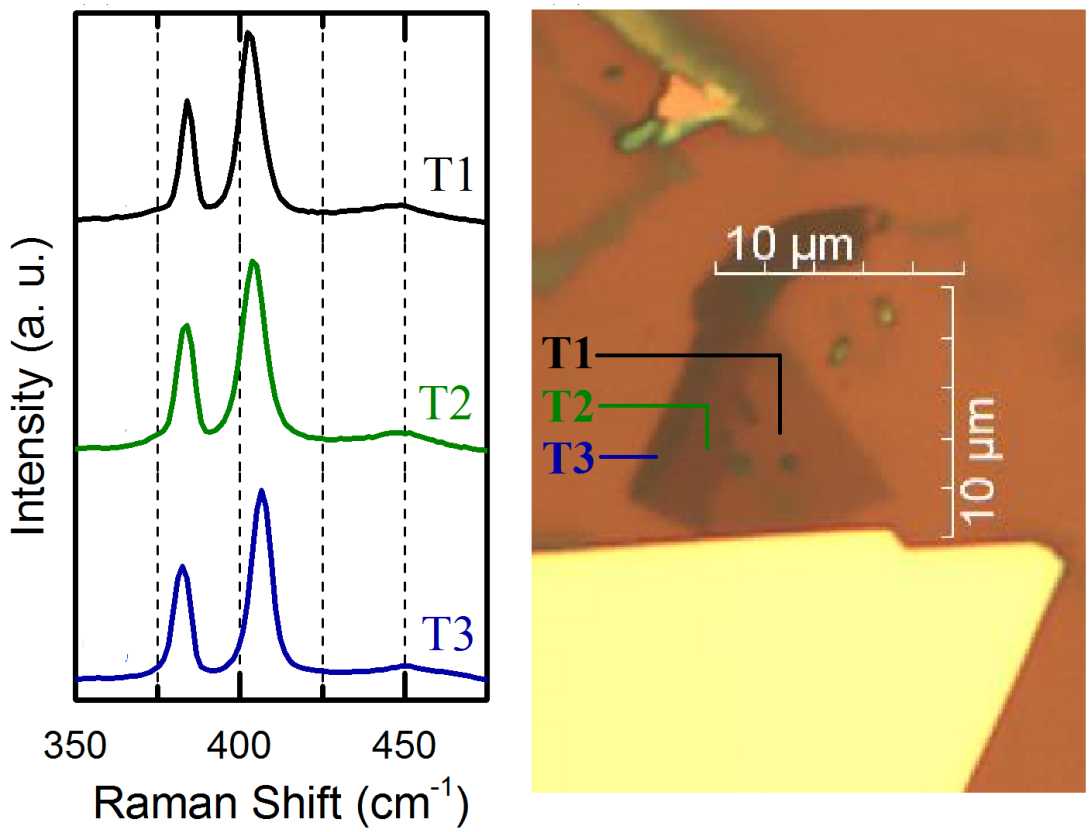

Figure 4.5 Raman spectrum of few-layers MoS_2 of the points T1, T2, and T3.

The deconvolution of the Raman spectra of MoS_2 samples are shown in Figure 4.6. Starting with the first-order bands, comparing our results with [48] (which differs less than 1 cm^{-1}) gives the first evidence that T1, T2, and T3 are single layer, bilayer, and trilayer, respectively. The data from the adjust shows that the E′ band redshift while increasing the number of layers, and the A_1' band blueshift.

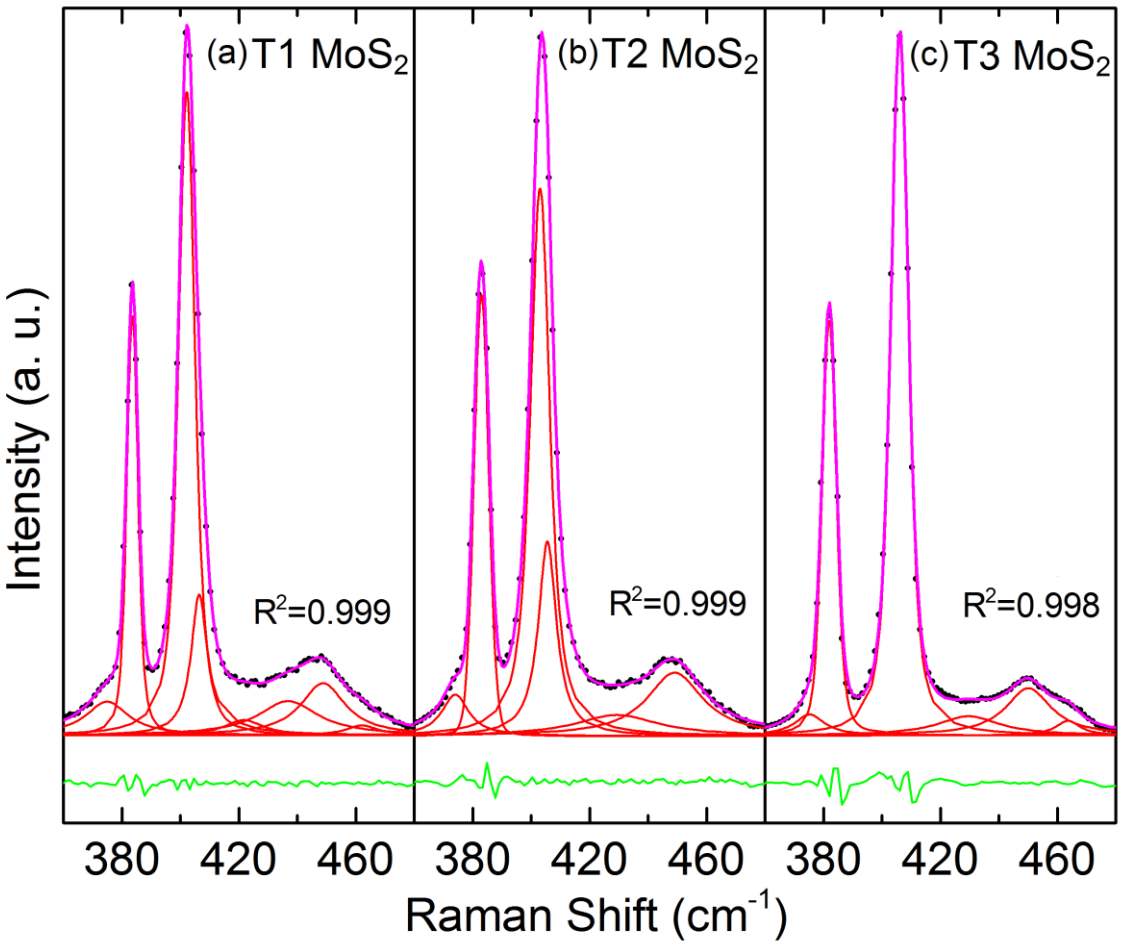

Figure 4.6 Fitted curves (red) with the data (black points) along with the residual (green) and its cumulative fitting curve o (magenta) for the points: **(a)** T1, **(b)** T2, and **(c)** T3, for few-layers MoS_2.

Small bands are seen around 450 cm^{-1} and in form of shoulders of the first-order bands. Following [34] for the case of single layer, we adjust this band with four Lorentzian for the band appearing in the region 420-280 cm^{-1} (2LA(K/M) band). The lower frequency band that appears next to the E′ band was reported in [49] as the LO_2(M) band.

The band at the right side of the A_1' band was also reported in [49] as the contribution of the ZO_2(M) phonon mode. Note that this band cannot be distinguish from the A_1' band for the case of trilayer. The bands appearing in 420-280 cm^{-1} for bilayer and trilayer has not been studied in detail. However, we present a proposal for its fitting.

4.3. Few-layers tungsten disulfide (WS_2)

The Raman spectra of samples of tungsten disulfide (WS_2) are shown in Figure 4.7 for different points. Since the bandgap lies around 2 eV (see Figures 2.14 and 2.18), the Raman scattering will be non-resonant. This make the contributions of the first-order bands the most prominent. The E′ band is seen around 350 cm^{-1}, and the A_1' band around 420 cm^{-1}. A small shoulder in the lower frequency side of the E′ band is appreciable.

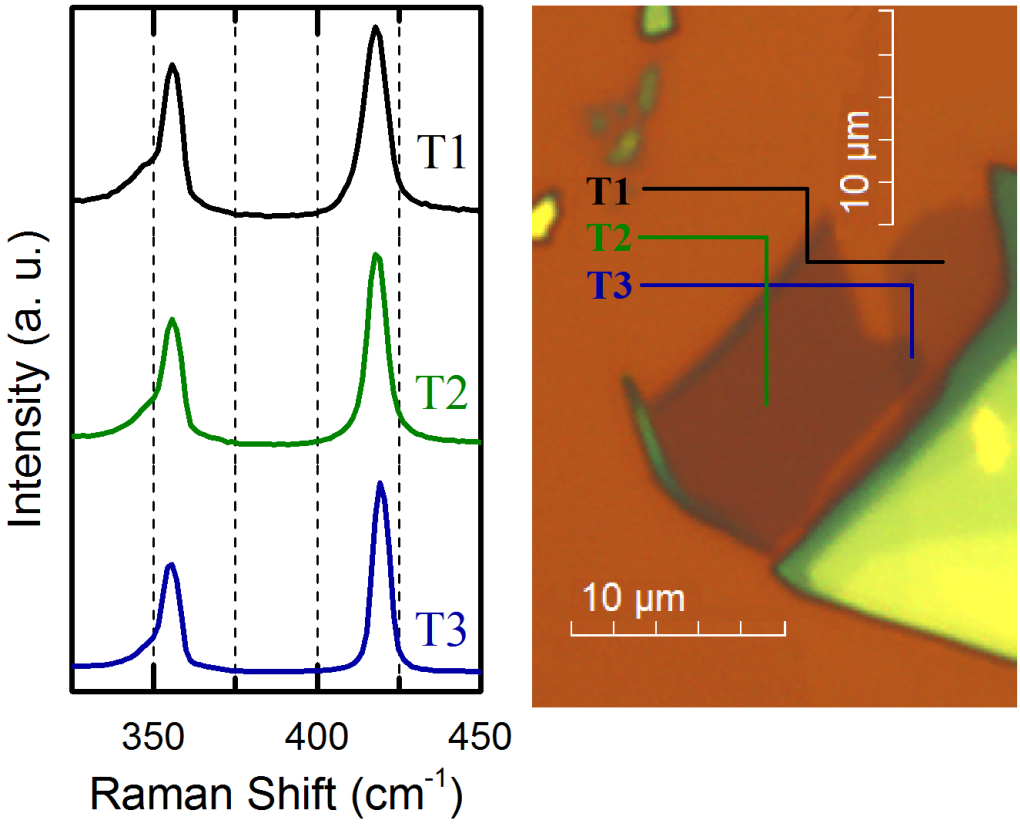

Figure 4.7 Raman spectrum of few-layers WS_2 of the points T1, T2, and T3.

The Raman spectra of WS_2 is analyzed in Figure 4.8. The same trend of redshift of the E′ band, and blueshift of the A_1' is observed. Comparing our results with [50], we find the evidence that T1, T2 and T3, correspond to single layer, bilayer, and trilayer, respectively. The intensity ratio of the first-order bands is also reported in the same work, which resembles our data.

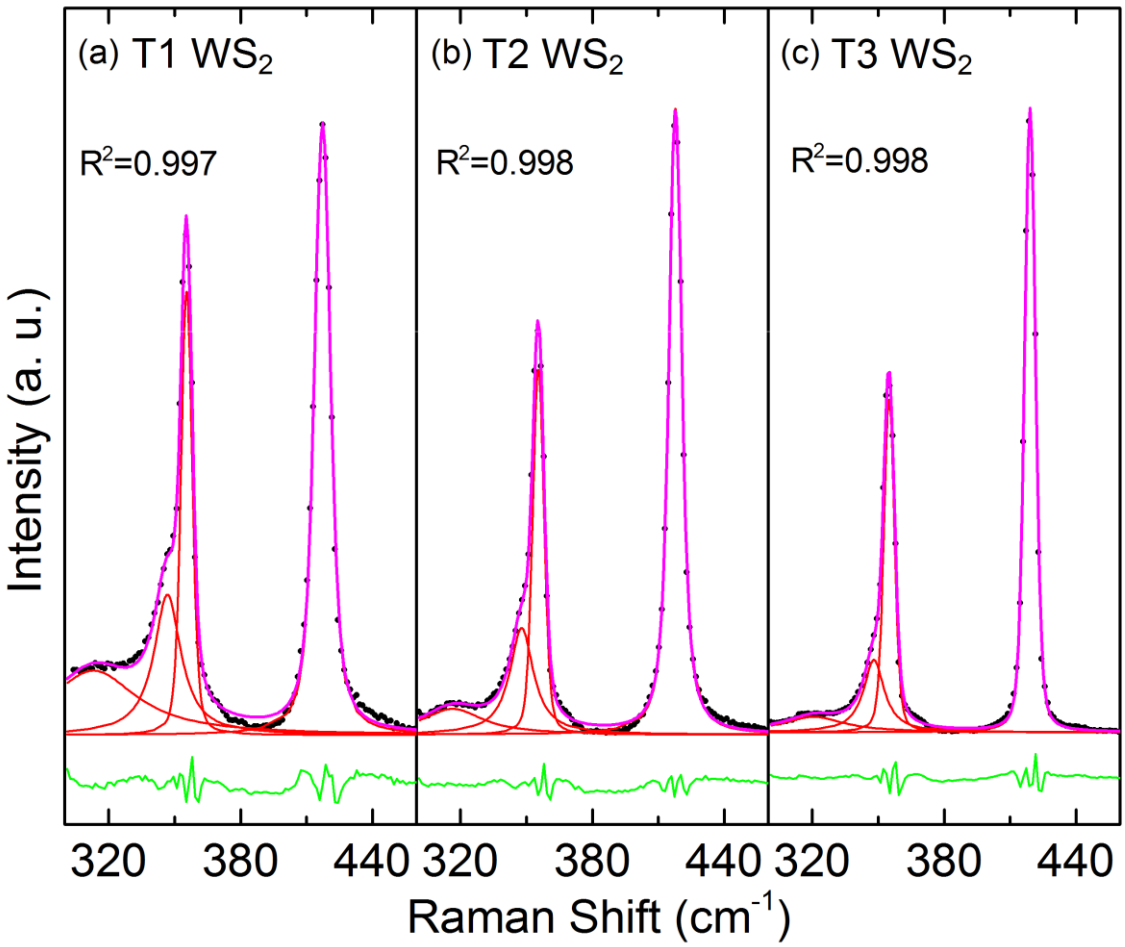

Figure 4.8 Fitted curves (red) with the data (black points) along with the residual (green) and its cumulative curve of the adjust (magenta) for the points: **(a)** T1, **(b)** T2, and **(c)** T3, for few-layers WS_2.

Analyzing the small contributions in the right side of the spectra, they fit to two Lorentzian curves. Those phonon contributions were attributed to the $TO_1(M)$ and $TO_2(M)$ phonons for the bands around 310 cm^{-1} and 350 cm^{-1}, respectively [49]. The small frequency difference of our data comes from the fact that our excitation source is different. Those bands are, perhaps, dependent on the laser energy. A detailed study of those bands is still lacking.

4.4. Few-layers molybdenum diselenide ($MoSe_2$)

Figure 4.9 shows the spectra for the Raman scattering for the molybdenum diselenide ($MoSe_2$). These spectra are non-resonant because the bandgap of $MoSe_2$ is around 1.6 eV (see Figure 2.14). A single main contribution is seen around 250 cm^{-1}. This sharp band correspond to the A_1' band. Although, its contribution is weak, the band around 280 cm^{-1} correspond to the E' band. Additional small bands are seen in the range of 300-450 cm^{-1}. Resonant studies of $MoSe_2$ are lacking, but the most recent work can be found in [51].

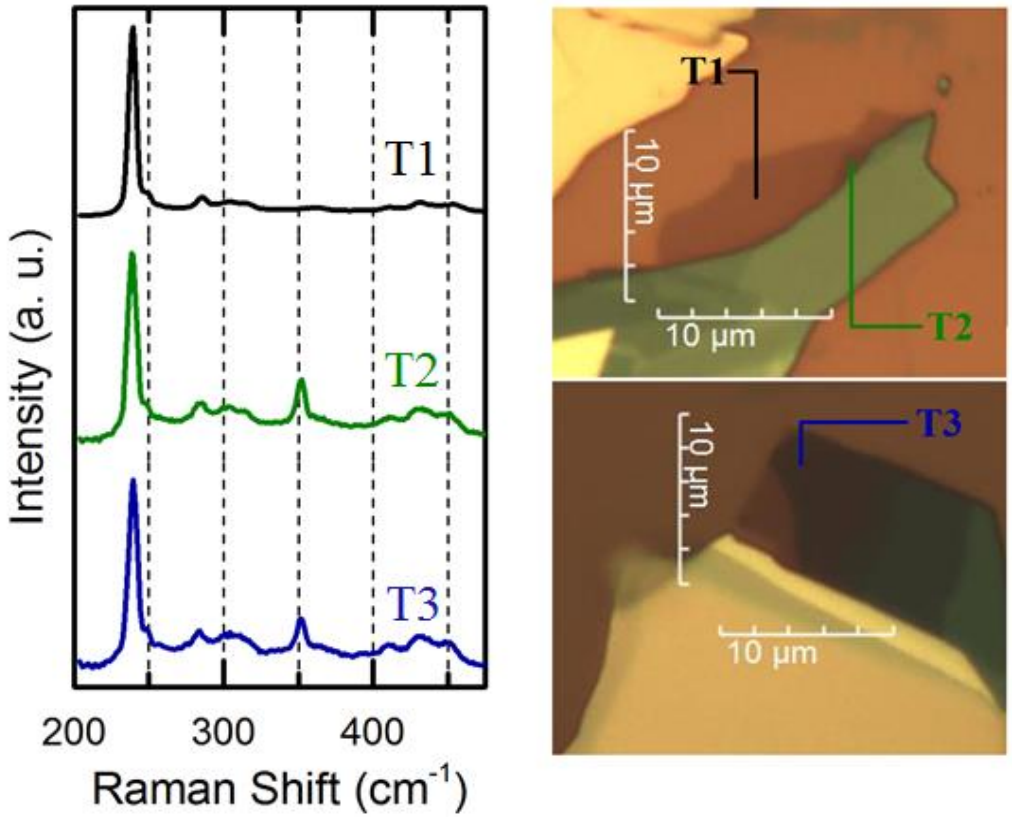

Figure 4.9 Raman spectrum of few-layers $MoSe_2$ of the points T1, T2, and T3.

The deconvolution of all contributions of the spectra shows a richer spectrum compared to the rest of the TMDCs. Starting with the first-order bands, we see that the E' band redshift, and the A_1' band blueshift, with increasing the thickness of the material (see contrast in Figure 4.7). A first evidence that T1 correspond to single layer, is that the data presented in [51] matches ours. For the points T2 and T3, we make use of the contrast of the

sample and the separation, which now decrease, because the E′ band is in the higher frequency side, and the A_1' band in the low frequency side. We can safely assume, with help of the image of the sample, that T2 and T3 are bilayer and trilayer.

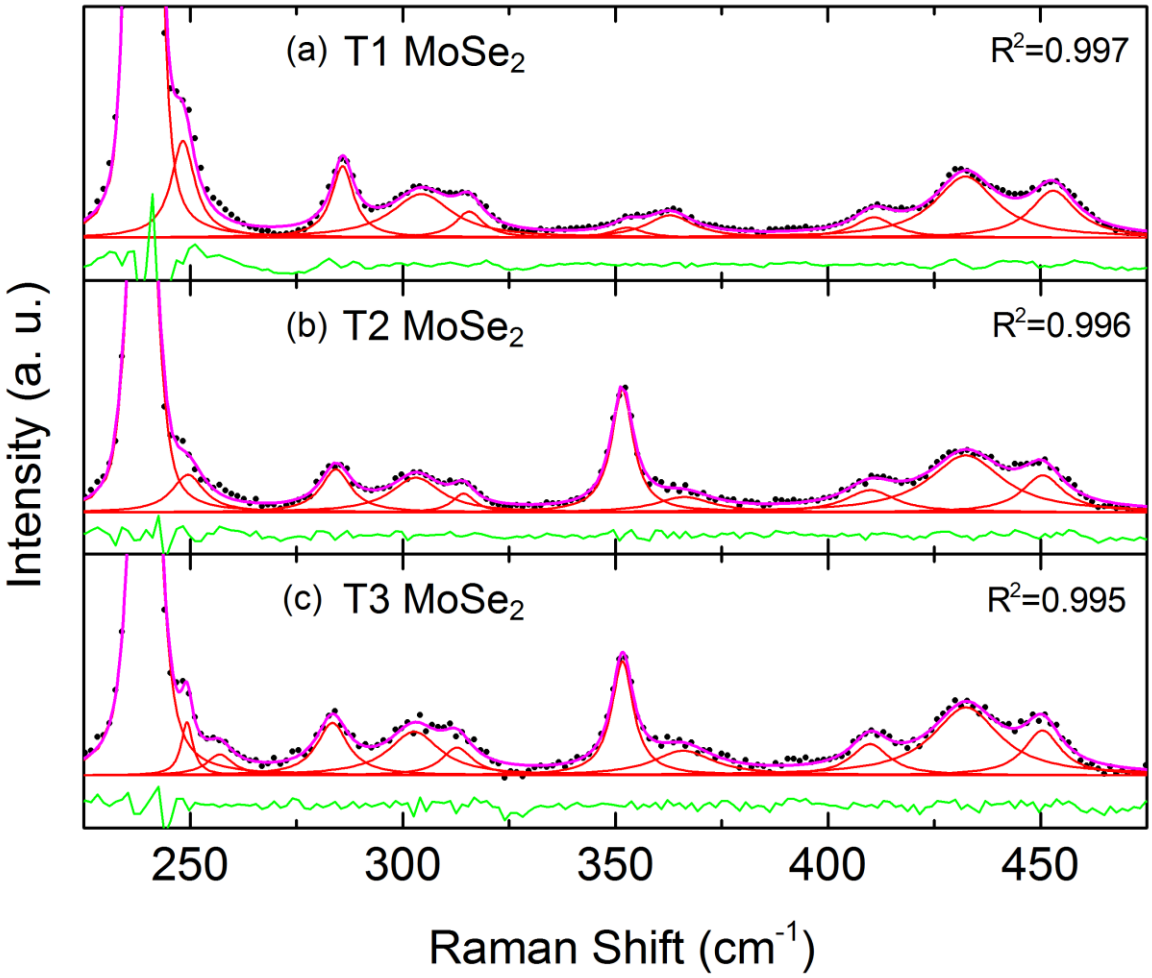

Figure 4.10 Fitted curves (red) with the data (black points) along with the residual (green) and its cumulative curve of the adjust (magenta) for the points: **(a)** T1, **(b)** T2, and **(c)** T3, for few-layers $MoSe_2$.

A summary of the phonon assignment for the bands in the range of 300-450 cm^{-1} is found in [51]. We note that these bands stay in the same frequency and lineshape for all thickness. We can, nonetheless, see that the band around 350 cm^{-1} becomes less intense for the case of the point T1, making this band an additional feature to distinguish a single layer.

4.5. Few-layers tungsten diselenide (WSe_2)

For tungsten diselenide, the Raman spectra are shown in Figure 4.11. In ab initio calculations reported in [52], it was shown that the first-order bands are degenerate. This means that we should not distinguish the E′ band and the A_1' band. This single, degenerate band appears around 250 cm^{-1}. Smaller contributions around this band are also observed. Additional weak bands are seen in the range of 300-450 cm^{-1}. Again, these spectra are non-resonant, because the bandgap for WSe_2 is around 1.6 eV (see Figure 2.14).

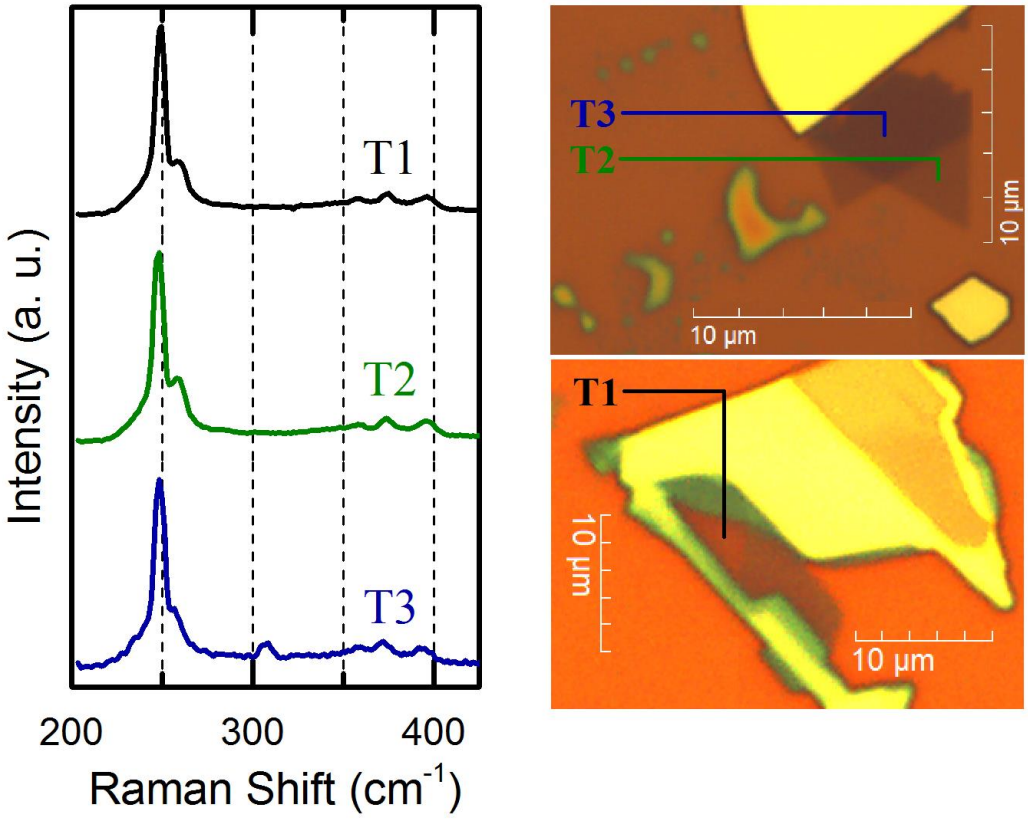

Figure 4.11 Raman spectrum of few-layers WSe_2 of the points T1, T2, and T3.

The deconvolution of the bands, as shown in Figure 4.12, shows that we can distinguish the E′ band and the A_1' band. This result could be explained by unintentional strains in the sample [53]. Due to this degeneracy, it is complicated to observe the separation of the first-order bands. However, comparing our results with [49], demonstrates that T1 is a single layer. Determining the thickness of T2 and T3 is difficult, and it requires additional

characterization tools, like photoluminescence (PL) or atomic force microscopy (AFM). However, if we see the contrast in Figure 4.11, it is relatively safe to assume that at least, T2 is bilayer.

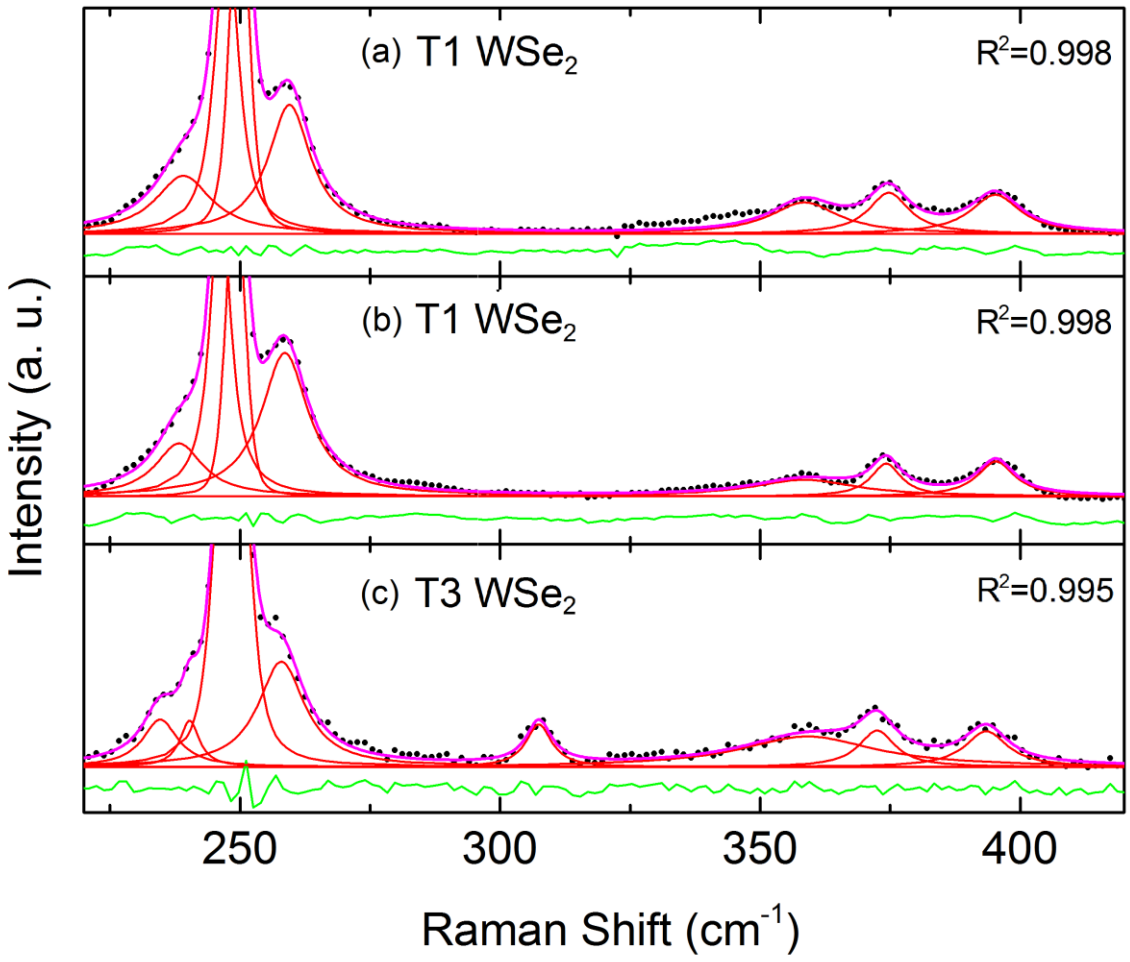

Figure 4.12 Fitted curves (red) with the data (black points) along with the residual (green) and its cumulative curve of the adjust (magenta) for the points: **(a)** T1, **(b)** T2, and **(c)** T3, for few-layers WSe_2.

The bands around 350-400 cm^{-1} were assigned in [49] as the 3TA(M) LO_2(M)+LA(M), and 3LA(M) band, from lower to higher frequency, respectively. These bands demonstrate that in WSe_2, third-order bands appear. The small band that appear for T3 around 310 cm^{-1} has been not reported yet.

5. Discussion and conclusion

In this last chapter, we will review the discussion of the results obtained in chapter 4 and compare them with results reported in recent works. Even though the assignation, position (frequency), and width differs among most works on the subject, it is worth making a comparation of these results with the ones obtained in this study to highlight insights from selected authors about the phonon assignments of higher-order scattering photons.

5.1. Discussion of few-layers graphene

The measurement shows that the only band seen was the E_{2g} band. From equation (2.13), we see that for bilayer graphene this band is called E_g instead. For trilayer, it is a combination of the modes E' and E''. However, as mention in section 2.2.4, we used the representation from the building block (single layer) to save notation. The modes A_{1g} (from bilayer) and A_1' (from trilayer) were not detected due to our limited rejection of the Rayleigh scattering, because they appear around ~90 cm^{-1} [54].

In graphene, the most effective way to determine the number of layers is the deconvolution of the 2TO(K) band. In early studies the intensity ratio of the E_{2g} and the 2TO(K) band was used. However, this is not as effective, because this ratio may vary if unintentional doping or strain is made on the sample [42]. Furthermore, as mention in [55], in turbostratic graphite, which the stacking of the graphene layers is rotationally random with respect one another, gives a Raman spectrum that look much like that for single layer graphene. Making the intensity ratio, not as trustworthy.

It is imperative to say, that the identification of the number of layers by Raman spectroscopy is well stablished only for graphene samples that have the AB stacking for the case of bilayer, and ABA and ABC stacking for trilayer. Graphene samples made by exfoliation of highly oriented pyrolytic graphite lead to graphene layers that have predominantly the AB, ABA, and ABC stacking configuration [24].

As mention in last chapter, the redshift of the E_{2g} band was explained by assuming that the sample were suspended, or by an increase in temperature due to the high laser power [56]. A shift in all spectra could explain this, but it was discarded because the position of the TO(K) and 2TO(K) band were in the same frequency (with difference less than 1 cm^{-1}) that the reported in [22-24], considering the dispersion of each band. Also, the position of the band from the substrate was verified.

The TO(K)+LA(K) band were reported in [24, 45]. A detailed deconvolution was only made for single layer, leaving the bilayer and trilayer yet to be stablished. We used four curves for the bilayer, and six curves for the trilayer. Another band that need further study is the 2LO(Γ) band. This band is reported in most studies of Raman spectrum of graphene, but its analyzing is poor or null.

5.2. Discussion of few-layers TMDCs

In TMDCs, it was shown that the separation of the first-order bands (E' and A_1') were used to unambiguously distinguish the number of layers of MoS_2, WS_2 and $MoSe_2$. In WSe_2, due the degeneracy of these bands, it almost impossible to use the same method. In general, the number of layers of the semiconducting family of TMDCs has been well stablished with photoluminescence (PL) measurements [57]. This is since the bandgap becomes direct in the case of single layer.

Nevertheless, using Raman spectroscopy to try to determine the number of layers can answer fundamental questions about the material, like the interlayer interaction. This interlayer interaction appears to affect the in-plane and out-of-plane motion of the atoms. Stacking layers reduce the frequency of the E' band and increase the frequency of the A_1' band. The origins of the shift have been identified as the influence of the neighboring layer on the effective restoring force on the atoms and the increase of dielectric screening of the long-range Coulomb interaction [58].

The small bands on TMDCs originated from 2-phonon and 3-phonon processes that appeared at low intensity compared to the first-order bands (1-phono) because our laser line

did not match, or was close, to the band gap of each material. To make a detailed analysis of these bands, different laser lines are required. The deconvolution proposal on this work, was done by comparing results of resonance studies [34, 49, 51]. It was also assumed that the bands had certain dispersion, justifying slight differences of band position due to the difference in excitation energy (laser line).

5.3. Conclusion and perspectives of 2D materials

Raman spectroscopy technique can provide characteristic spectral information of the sample under study. In two-dimensional materials, the first-order bands generated from 1-phonon processes correspond to motions of the atoms in-plane and out-of-plane. Note that in single layer graphene, there is no out-of-plane Raman active mode, like in 2D TMDCs. However, when stacking graphene layers, modes related to the motion of the atoms perpendicular to the plane appear, which are labeled with A_{1g} for bilayer and A_1' for trilayer. Despite this, these modes were not observed, as mention above.

The 2TO(K) band, which is from a 2-phonon process had an intensity comparable to the first-order band in graphene, which was explained in terms of the resonance condition This condition is satisfied in graphene for al laser lines in the visible spectrum. On the other hand, since not all excitation energies are resonant for 2D TMDCs, the second-order bands (or third-order), had a low intensity comparable to the first-order bands. Those features, which are fingerprints of the sample, are used to measure external effects on the sample.

Nonetheless, the spatial resolution of this technique is limited to the laser spot that generates the objective with the laser. A way of improving the spatial resolution is by Tip-enhanced Raman spectroscopy (TERS) [59], which reduce the spatial resolution in the orders of nanometers. This enchantment in the resolution makes the survey of external effects on the sample much more detailed.

Another limitation of the technique is the low intensity signal. This make the time acquisition of the Raman spectrum to take considerable amount of time. A technique called Coherent Anti-Stokes Raman spectroscopy (CARS) [60], addresses the vibration with

multiple photons, and produces a coherent signal. As a result, CARS is orders of magnitude stronger than Raman emissions. The perspective of implementing these new techniques to improve the Raman study of 2D materials, has the potential of revealing new features and new fundamental physics on these layered structures.

6. References

[1] K. Novoselov *et al*. "Nobel lecture: Graphene: Materials in the flatland*", Reviews of Modern Physics* **86**, 837 (2011).

[2] Z. Liu *et al*. "Functionalized graphene and other two-dimensional materials for photovoltaic devices: device design and processing". *Chemical Society Reviews* **44**, 5638 (2015).

[3] K. Mak *et al. "Atomically Thin MoS2: A New Direct-Gap Semiconductor". Physical Review Letters* **105**, 136805 (2010).

[4] G. Dimitrios *et al. "*Mechanical properties of graphene and graphene-based nanocomposites". *Progress in Materials Science* **90**, 75 (2017).

[5] K. Novoselov *et al.* "Electric Field Effect in Atomically Thin Carbon Films". *Science* **306**, 666 (2004).

[6] J. Yu *et al*. "Synthesis of high quality two-dimensional materials via chemical vapor deposition". *Chemical Science* **12**, 6705 (2015).

[7] X. Li *et al.* "Large-Area Graphene Single Crystals Grown by Low-Pressure Chemical Vapor Deposition of Methane on Copper". *Journal of the American Chemical Society* **133**, 2816 (2011).

[8] K. Kang *et al.* "High-mobility three-atom-thick semiconducting films with wafer-scale homogeneity". *Nature* **520**, 656 (2015).

[9] R. Singh *et al.* "Magnetism in graphene due to single-atom defects: dependence on the concentration and packing geometry of defects". *Journal of Physics: Condensed Matter* **21**, 196002 (2009*).*

[10] C. Ferarri *et al. "*Supplementary Information for "Raman spectroscopy as a versatile tool for studying the properties of graphene*". Nature Nanotechnology* **8**, 235 (2013*).*

[11] M. Y. Sfeir *et al.* "Optical Spectroscopy of Individual Single-Walled Carbon Nanotubes of Defined Chiral Structure". *Science* **312**, 554 (2006).

[12] C. Casiraghi *et al*. "Rayleigh Imaging of Graphene and Graphene Layers". *Nano Letters* **7**, 2711 (2007).

[13] S. Chakraborti *et al*. "Verification of the Rayleigh scattering cross section". *American Journal of Physics*. **75,** 824 (2007).

[14] P. Y. Yu & *M.* Cardona, *Fundamentals of Semiconductors* (2005).

[15] D. A. Long, *The Raman effect: A Unified Treatment of the Theory of Raman scattering by Molecules* (2002).

[16] N. Bonini *et al.* "Phonon Anharmonicities in Graphite and Graphene". *Physical Review Letters* **99**, 176802 (2007).

[17] M. Lazzeri *et al*. "Phonon linewidths and electron-phonon coupling in graphite and nanotubes". *Physical Review B* **73**, 155426 (2006).

[18] G. L. Frey *et al. "*Raman and resonance Raman investigation of MoS 2 nanoparticles." *Physical Review B* **60**, 2883 (1999).

[19] A. Jorio, R. Saito, G. Dresselhaus & M. S. Dresselhaus, *Raman Spectroscopy in Graphene Related Systems* (2011).

[20] K. Nakada *et al.* "DFT Calculation for Adatom Adsorption on Graphene". *Graphene Simulation* (2011).

[21] L. M. Malard *et al.* "Group-theory analysis of electrons and phonon in *N*-layer graphene systems". *Physical Review B* **79**, 125426 (2009).

[22] M. A. Pimenta *et al.* "Comparative Study of Raman Spectroscopy in Graphene and MoS_2-type Transition Metal Dichalcogenides". *Accounts of Chemical Research* **48**, 41 (2015).

[23] A. C. Ferrari *et al.* "Raman Spectroscopy as a versatile tool for studying the properties of graphene". *Nature Nanotechnology **8***, 235 (2013).

[24] T. A. Nguyen *et al.* "Excitation Energy Dependent Raman Signatures of ABA- and ABC-stacked Few-layer Graphene". *Scientific Reports* **4**, 4630 (2014).

[25] C. Bao *et al*. "Stacking-Dependent Electronic Structure of Trilayer Graphene Resolved by Nanospot Angle-Resolved Photoemission Spectroscopy". *Nano Letters* **17**, 1564 (2017).

[26] R. Roldán et al. "Electronic properties of single-layer and multilayer transition metal dichalcogenides MX2 (M = Mo, W and X = S, Se)". *Annalen der Physik* **526,** 347 (2014).

[27] A. V. Kobolov, *Two-dimensional Transition-Metal Dichalcogenides* (2016).

[28] Y. C. Cheng *et al.* "Spin-orbit-induced spin splitting in polar transition metal dichalcogenides monolayers". *A Letters Journal Exploring the Frontiers of Physics* **102**, 57001 (2013).

[29] G. B. Liu *et al.* "Three-band tight-binding model for monolayers of group-VIB transition metal dichalcogenides". *Physical Review B* **88**, 085433 (2013).

[30] A. Kumar et al. "Electronic structure of transition metal dichalcogenides monolayers 1H-MX2 (M = Mo, W; X = S, Se, Te)". *The European Physical Journal B* **85**, 186 (2012).

[31] J. Ribeiro-Soares *et al.* "Group theory analysis of phonons in two-dimensional transition metal dichalcogenides". *Physical Review B* **90**, 115438 (2014).

[32] J. Lee *et al.* "Resonance Raman effects in transition metal dichalcogenides". *Journal of Raman Spectroscopy* **49**, 66 (2017).

[33] N. T. McDevitt *et al.* "Disorder-induced low-frequency Raman bands observed in deposited MoS_2 films". *Applied Spectroscopy* **48**, 733 (1994).

[34] B. R. Carvalho *et al.* "Intervalley scattering by acoustic phonon in two-dimensional MoS_2 revealed by double-resonance Raman spectroscopy". *Nature Communications* **8**, 14670 (2017).

[35] J. N. Coleman *et al.* "Two-Dimensional Nanosheets Produced by Liquid Exfoliation of Layered Materials". *Science* **331**, 568 (2011).

[36] Y. Hernandez *et al.* "High-yield production of graphene by liquid-phase exfoliation of graphite". *Nature Nanotechnology* **3**, 563 (2008).

[37] P. Blake *et al.* "Making graphene visible". *Applied Physics Letter* **91**, 063124 (2007).

[38] M. M. Benameur *et al.* "Visibility of dichalcogenide nanolayers". *Nanotechnology* **22**, 125706 (2011).

[39] O. Lopez-Sanchez *et al.* "Ultrasensitive photodetectors based on monolayers MoS_2". *Nature Nanotechnology* **8**, 497 (2013).

[40] B. P. Asthana *et al.* "Deconvolution of the Lorentzian Linewidth and Determination of Fraction Lorentzian Character from the Observed Profile of a Raman Line by a Comparison Technique". *Applied Spectroscopy* **36**, 250 (1982).

[41] A. Das *et al.* “Raman spectroscopy of graphene on different substrates and influence of defects”. *Bulletin of Material Science* **31**, 579 (2008).

[42] Z. H. Ni *et al.* “Probing Charged Impurities in Suspended Graphene Using Raman Spectroscopy”. *American Chemical Society Nano* **3**, 569 (2009).

[43] Z. Luo *et al.* “Direct observation of inner and outer G′ band double-resonance Raman scattering in free standing graphene”. *Applied Physics Letter* **100**, 243107 (2012).

[44] C. Neumann *et al.* “Line shape of the Raman 2D peak of graphene in van der Waals heterostructures”. *Physica Status Solidi (b)* **253**, 2326 (2016).

[45] L. M. Malard *et al.* “Probing the electronic structure of bilayer graphene by Raman scattering”. *Physical Review B* **76**, 201401 (2007).

[46] P. May *et al.* “Signature of the two-dimensional phonon dispersion in graphene probed by double-resonant Raman scattering”. *Physical Review B* **87**, 075402 (2013).

[47] L. G. Cançado *et al.* “Quantifying Defects in Graphene via Raman Spectroscopy at Different Excitation Energies”. *Nano Letters* **11**, 3190 (2011).

[48] H. Li *et al.* “From Bulk to Monolayer MoS_2: Evolution of Raman Scattering”. *Advanced Functional Materials* **22**, 1385 (2012).

[49] X. Zhang *et al.* “Phonon and Raman scattering of two-dimensional transition metal dichalcogenides from monolayer, multilayer to bulk material”. *Chemical Society Review* **44**, 2757 (2015).

[50] A. Berkdemir *et al.* “Identification of individual and few layers of WS_2 using Raman Spectroscopy”. *Scientific Report* **3**, 1755 (2013).

[51] P. Soubelet *et al*. “Resonance effects in the Raman scattering of monolayer and few-layer $MoSe_2$”. *Physical Review B* **93**, 155407 (2016).

[52] H. Terrones *et al.* “New First Order Raman-active Modes in Few Layered Transition Metal Dichalcogenides”. *Scientific Reports* **4**, 4215 (2014).

[53] H. Sahin *et al.* “Anomalous Raman spectra and thickness-dependent electronic properties of WSe2”. *Physical Review B* **87**, 165409 (2013).

[54] S. K. Saha *et al.* “Phonons in few-layer graphene and interplanar interaction: A first-principles study”. *Physical Review* B **78**, 165421 (2008).

[55] L. M. Malard *et al.* “Raman spectroscopy in graphene”. *Physics Report* **473**, 51 (2009).

[56] I. Calizo *et al.* “Temperature Dependence of the Raman Spectra of Graphene and Graphene Multilayers”. *Nano Letters* **7**, 2645 (2007).

[57] P. Tonndorf *et al.* “Photoluminescence emission and Raman response of monolayer MoS_2, $MoSe_2$, and WSe_2”. *Optic Express* **21**, 4908 (2013).

[58] A. Molina-Sanchez *et al.* “Phonons in single-layer and few-layer MoS_2 and WS_2”. *Physical Review B* **84**, 155413 (2011).

[59] P. Verma *et al.* “Tip-Enhanced Raman Spectroscopy: Technique and Recent Advances”. *Chemical Review* **117**, 6447 (2017).

[60] J. Brocious *et al.* “Lighting up micro-structured materials with four-wave mixing microscopy”. *Materials Today* **16**, 9 (2013).

A. Fitted parameters used for graphene

In this appendix, the parameters used to fit the curves of section 4.1, corresponding to few-layers graphene, are displayed below. The assignation of the bands is according to [19], [21-24], [44-47], and [55]. The parameters are frequency (ω), full width at half maximum (FWHM), and intensity (I).

Table A.1 Parameters used for the fitting of T1 graphene in the range of 1300-1700 cm^{-1}.

Band	Parameter	Value
TO(K)	ω (cm^{-1})	1344.37
	FWHM (cm^{-1})	11.82
	I	585.87
	ω (cm^{-1})	1353.64
	FWHM (cm^{-1})	18.48
	I	383.15
External factors	ω (cm^{-1})	1549.13
	FWHM (cm^{-1})	4.61
	I	477.71
$E_{2g}(\Gamma)$	ω (cm^{-1})	1576.31
	FWHM (cm^{-1})	13.51
	I	2348.18
LO(Γ)	ω (cm^{-1})	1619.08
	FWHM (cm^{-1})	10.37
	I	158.74

Table A.2 Parameters used for the fitting of T2 graphene in the range of 1300-1700 cm^{-1}.

Band	Parameter	Value
External factors	ω (cm^{-1})	1549.13
	FWHM (cm^{-1})	4.60
	I	409.65
$E_{2g}(\Gamma)$	ω (cm^{-1})	1574.36
	FWHM (cm^{-1})	13.15
	I	15080.80
LO(Γ)	ω (cm^{-1})	1616.62
	FWHM (cm^{-1})	7.10
	I	91.15

Table A.3 Parameters used for the fitting of T3 graphene in the range of 1300-1700 cm^{-1}.

Band	Parameter	Value
External factors	ω (cm^{-1})	1549.13
	FWHM (cm^{-1})	4.60
	I	344.31
$E_{2g}(\Gamma)$	ω (cm^{-1})	1573.90
	FWHM (cm^{-1})	12.63
	I	12788.73

Table A.4 Parameters used for the fitting of T4 graphene in the range of 1300-1700 cm^{-1}.

Band	Parameter	Value
External factors	ω (cm^{-1})	1549.13
	FWHM (cm^{-1})	4.60
	I	374.27
$E_{2g}(\Gamma)$	ω (cm^{-1})	1574.94
	FWHM (cm^{-1})	13.80
	I	20047.45

Table A.5 Parameters used for the fitting of T1 graphene in the range of 2300-3300 cm^{-1}.

Band	Parameter	Value
TO(K)+LA(K)	ω (cm^{-1})	2443.64
	FWHM (cm^{-1})	19.80
	I	464.13
	ω (cm^{-1})	2466.23
	FWHM (cm^{-1})	31.86
	I	149.76
2TO(K)	ω (cm^{-1})	2698.84
	FWHM (cm^{-1})	22.99
	I	11341.03
2LO(Γ)	ω (cm^{-1})	3248.19
	FWHM (cm^{-1})	11.35
	I	967.61

Table A.6 Parameters used for the fitting of T2 graphene in the range of 2300-3300 cm^{-1}.

Band	Parameter	Value
TO(K)+LA(K)	ω (cm^{-1})	2427.81
	FWHM (cm^{-1})	9.60
	I	398.40
	ω (cm^{-1})	2435.51
	FWHM (cm^{-1})	12.31
	I	381.18
	ω (cm^{-1})	2447.13
	FWHM (cm^{-1})	20.04
	I	694.29
	ω (cm^{-1})	2466.32
	FWHM (cm^{-1})	40.96
	I	277.02
2TO(K)	ω (cm^{-1})	2673.47
	FWHM (cm^{-1})	24.00
	I	1949.21
	ω (cm^{-1})	2699.97
	FWHM (cm^{-1})	24.00
	I	10836.10
	ω (cm^{-1})	2719.49
	FWHM (cm^{-1})	24.00
	I	10408.66
	ω (cm^{-1})	2731.18
	FWHM (cm^{-1})	24.00
	I	9203.66
2LO(Γ)	ω (cm^{-1})	3246.80
	FWHM (cm^{-1})	11.94
	I	3027.65

Table A.7 Parameters used for the fitting of T3 graphene in the range of 2300-3300 cm^{-1}.

Band	Parameter	Value
TO(K)+LA(K)	ω (cm^{-1})	2422.29
	FWHM (cm^{-1})	6.20
	I	193.69
	ω (cm^{-1})	2428.64
	FWHM (cm^{-1})	9.11
	I	331.58
	ω (cm^{-1})	2436.64
	FWHM (cm^{-1})	13.23
	I	352.70
	ω (cm^{-1})	2448.15
	FWHM (cm^{-1})	21.04
	I	453.35
	ω (cm^{-1})	2468.69
	FWHM (cm^{-1})	40.59
	I	187.11
2TO(K)	ω (cm^{-1})	2670.22
	FWHM (cm^{-1})	24.00
	I	790.38
	ω (cm^{-1})	2687.22
	FWHM (cm^{-1})	24.00
	I	1373.77
	ω (cm^{-1})	2700.85
	FWHM (cm^{-1})	24.00
	I	6649.41
	ω (cm^{-1})	2717.41
	FWHM (cm^{-1})	24.00
	I	5563.87
	ω (cm^{-1})	2730.30
	FWHM (cm^{-1})	24.00
	I	6586.50
	ω (cm^{-1})	2742.06
	FWHM (cm^{-1})	24.00
	I	2700.85
2LO(Γ)	ω (cm^{-1})	3245.67
	FWHM (cm^{-1})	8.91
	I	2428.26

Table A.8 Parameters used for the fitting of T4 graphene in the range of 2300-3300 cm^{-1}.

Band	Parameter	Value
TO(K)+LA(K)	ω (cm^{-1})	2423.88
	FWHM (cm^{-1})	8.77
	I	375.50
	ω (cm^{-1})	2430.96
	FWHM (cm^{-1})	10.26
	I	464.59
	ω (cm^{-1})	2439.45
	FWHM (cm^{-1})	13.90
	I	551.82
	ω (cm^{-1})	2450.55
	FWHM (cm^{-1})	21.44
	I	625.79
	ω (cm^{-1})	2470.13
	FWHM (cm^{-1})	43.98
	I	308.87
2TO(K)	ω (cm^{-1})	2672.50
	FWHM (cm^{-1})	24.00
	I	843.19
	ω (cm^{-1})	2688.17
	FWHM (cm^{-1})	24.00
	I	2400.88
	ω (cm^{-1})	2703.34
	FWHM (cm^{-1})	24.00
	I	10238.77
	ω (cm^{-1})	2716.49
	FWHM (cm^{-1})	24.00
	I	6465.28
	ω (cm^{-1})	2730.85
	FWHM (cm^{-1})	24.00
	I	9925.94
	ω (cm^{-1})	2743.57
	FWHM (cm^{-1})	24.00
	I	5996.76
2LO(Γ)	ω (cm^{-1})	3246.90
	FWHM (cm^{-1})	11.16
	I	3473.61

B. Fitted parameters used for 2D TMDCs

In this appendix, the parameters used to fit the curves section 4.2, 4.3, 4.4, and 4.5 corresponding to few-layers MoS_2, few-layers WS_2, few-layers $MoSe_2$, and few-layers WSe_2 respectively, are displayed below. The assignation of the bands is according to [49] and [51]. The parameters are frequency (ω), full width at half maximum (FWHM), and intensity (I).

Table B.1 Parameters used for the fitting of T1 MoS_2.

Band	Parameter	Value
E'(Γ)	ω (cm^{-1})	383.56
	FWHM (cm^{-1})	4.59
	I	3497.79
A'_1(Γ)	ω (cm^{-1})	402.19
	FWHM (cm^{-1})	6.72
	I	5367.61
LO_2(M)	ω (cm^{-1})	374.92
	FWHM (cm^{-1})	17.79
	I	282.11
ZO_2(M)	ω (cm^{-1})	406.42
	FWHM (cm^{-1})	6.75
	I	1176.60
2LA(K/M)	ω (cm^{-1})	421.74
	FWHM (cm^{-1})	16.10
	I	128.28
	ω (cm^{-1})	436.86
	FWHM (cm^{-1})	25.16
	I	286.65
	ω (cm^{-1})	448.78
	FWHM (cm^{-1})	18.53
	I	435.92
	ω (cm^{-1})	462.12
	FWHM (cm^{-1})	13.27
	I	83.61

Table B.2 Parameters used for the fitting of T2 MoS_2.

Band	Parameter	Value
E'(Γ)	ω (cm^{-1})	382.96
	FWHM (cm^{-1})	5.98
	I	2912.84
A'_1(Γ)	ω (cm^{-1})	403.02
	FWHM (cm^{-1})	7.92
	I	3618.79
LO_2(M)	ω (cm^{-1})	374.01
	FWHM (cm^{-1})	11.21
	I	275.00
ZO_2(M)	ω (cm^{-1})	405.53
	FWHM (cm^{-1})	7.50
	I	1286.06
2LA(K/M)	ω (cm^{-1})	429.35
	FWHM (cm^{-1})	34.75
	I	140.08
	ω (cm^{-1})	449.11
	FWHM (cm^{-1})	23.44
	I	419.42

Table B.3 Parameters used for the fitting of T3 MoS_2.

Band	Parameter	Value
E'(Γ)	ω (cm^{-1})	381.95
	FWHM (cm^{-1})	5.80
	I	6546.22
A'_1(Γ)	ω (cm^{-1})	406.04
	FWHM (cm^{-1})	7.17
	I	11029.19
LO_2(M)	ω (cm^{-1})	375.23
	FWHM (cm^{-1})	12.43
	I	332.51
2LA(K/M)	ω (cm^{-1})	429.67
	FWHM (cm^{-1})	25.93
	I	305.11
	ω (cm^{-1})	450.06
	FWHM (cm^{-1})	18.94
	I	748.31
	ω (cm^{-1})	463.62
	FWHM (cm^{-1})	10.12
	I	233.48

Table B.4 Parameters used for the fitting of T1 WS_2.

Band	Parameter	Value
E'(Γ)	ω (cm^{-1})	355.41
	FWHM (cm^{-1})	6.06
	I	1845.79
A'_1(Γ)	ω (cm^{-1})	417.21
	FWHM (cm^{-1})	8.69
	I	2528.84
TO_1(M)	ω (cm^{-1})	313.07
	FWHM (cm^{-1})	48.17
	I	268.14
TO_2(M)	ω (cm^{-1})	346.68
	FWHM (cm^{-1})	14.86
	I	584.21

Table B.5 Parameters used for the fitting of T2 WS_2.

Band	Parameter	Value
E'(Γ)	ω (cm^{-1})	355.40
	FWHM (cm^{-1})	6.13
	I	3661.65
A'_1(Γ)	ω (cm^{-1})	417.71
	FWHM (cm^{-1})	7.04
	I	6285.73
TO_1(M)	ω (cm^{-1})	316.39
	FWHM (cm^{-1})	33.60
	I	258.59
TO_2(M)	ω (cm^{-1})	347.79
	FWHM (cm^{-1})	12.97
	I	1071.02

Table B.6 Parameters used for the fitting of T3 WS_2.

Band	Parameter	Value
E'(Γ)	ω (cm^{-1})	354.92
	FWHM (cm^{-1})	5.76
	I	5607.29
A'_1(Γ)	ω (cm^{-1})	419.01
	FWHM (cm^{-1})	5.90
	I	10519.76
TO_1(M)	ω (cm^{-1})	320.62
	FWHM (cm^{-1})	33.81
	I	260.40
TO_2(M)	ω (cm^{-1})	348.00
	FWHM (cm^{-1})	11.34
	I	1220.54

Table B.7 Parameters used for the fitting of T1 $MoSe_2$.

Band	Parameter	Value
$A'_1(\Gamma)$	ω (cm^{-1})	238.99
	FWHM (cm^{-1})	5.86
	I	15429.73
E'(Γ)	ω (cm^{-1})	285.88
	FWHM (cm^{-1})	6.36
	I	776.26
Not assigned yet	ω (cm^{-1})	248.30
	FWHM (cm^{-1})	6.79
	I	1050.85
2LA(K/M)	ω (cm^{-1})	304.43
	FWHM (cm^{-1})	17.44
	I	474.36
	ω (cm^{-1})	315.63
	FWHM (cm^{-1})	7.91
	I	284.33
$A''_2(\Gamma)$	ω (cm^{-1})	352.79
	FWHM (cm^{-1})	9.02
	I	109.54
A'_1(M)+LA(M)	ω (cm^{-1})	362.87
	FWHM (cm^{-1})	13.45
	I	243.35
TA(M)+2LA(M)	ω (cm^{-1})	410.83
	FWHM (cm^{-1})	11.41
	I	221.45
E'(M)+LA(M)	ω (cm^{-1})	432.37
	FWHM (cm^{-1})	17.60
	I	665.59
3LA(M)	ω (cm^{-1})	452.98
	FWHM (cm^{-1})	13.03
	I	510.94

Table B.8 Parameters used for the fitting of T2 $MoSe_2$.

Band	Parameter	Value
$A'_1(\Gamma)$	ω (cm^{-1})	238.69
	FWHM (cm^{-1})	7.02
	I	2084.42
E'(Γ)	ω (cm^{-1})	284.26
	FWHM (cm^{-1})	8.53
	I	188.41
Not assigned yet	ω (cm^{-1})	249.49
	FWHM (cm^{-1})	9.12
	I	164.59
2LA(K/M)	ω (cm^{-1})	303.12
	FWHM (cm^{-1})	14.36
	I	151.71
	ω (cm^{-1})	314.29
	FWHM (cm^{-1})	6.47
	I	81.93
$A''_2(\Gamma)$	ω (cm^{-1})	351.64
	FWHM (cm^{-1})	6.20
	I	537.44
A'_1(M)+LA(M)	ω (cm^{-1})	366.20
	FWHM (cm^{-1})	16.18
	I	67.09
TA(M)+2LA(M)	ω (cm^{-1})	409.97
	FWHM (cm^{-1})	14.28
	I	97.16
E'(M)+LA(M)	ω (cm^{-1})	432.41
	FWHM (cm^{-1})	20.89
	I	249.55
3LA(M)	ω (cm^{-1})	450.49
	FWHM (cm^{-1})	11.69
	I	162.35

Table B.9 Parameters used for the fitting of T3 $MoSe_2$.

Band	Parameter	Value
$A'_1(\Gamma)$	ω (cm^{-1})	239.35
	FWHM (cm^{-1})	6.93
	I	1361.90
E'(Γ)	ω (cm^{-1})	283.46
	FWHM (cm^{-1})	8.90
	I	122.51
Not assigned yet	ω (cm^{-1})	249.25
	FWHM (cm^{-1})	3.35
	I	124.06
	ω (cm^{-1})	256.95
	FWHM (cm^{-1})	7.58
	I	48.82
2LA(K/M)	ω (cm^{-1})	302.69
	FWHM (cm^{-1})	14.60
	I	101.88
	ω (cm^{-1})	312.77
	FWHM (cm^{-1})	8.90
	I	64.76
$A''_2(\Gamma)$	ω (cm^{-1})	351.66
	FWHM (cm^{-1})	6.22
	I	266.12
A'_1(M)+LA(M)	ω (cm^{-1})	365.95
	FWHM (cm^{-1})	17.19
	I	57.49
TA(M)+2LA(M)	ω (cm^{-1})	409.88
	FWHM (cm^{-1})	10.80
	I	73.24
E'(M)+LA(M)	ω (cm^{-1})	432.43
	FWHM (cm^{-1})	19.20
	I	158.70
3LA(M)	ω (cm^{-1})	450.42
	FWHM (cm^{-1})	10.50
	I	104.66

Table B.10 Parameters used for the fitting of T1 WSe_2.

Band	Parameter	Value
E'(Γ)	ω (cm^{-1})	247.44
	FWHM (cm^{-1})	5.56
	I	2647.78
A'_1(Γ)	ω (cm^{-1})	249.90
	FWHM (cm^{-1})	4.43
	I	3188.62
LA(M)+TA(M)	ω (cm^{-1})	239.14
	FWHM (cm^{-1})	13.17
	I	519.72
A''_2(M)	ω (cm^{-1})	259.52
	FWHM (cm^{-1})	9.99
	I	1155.02
2LA(M)	ω (cm^{-1})	358.50
	FWHM (cm^{-1})	16.00
	I	281.49
LO_2(M)+LA(M)	ω (cm^{-1})	374.74
	FWHM (cm^{-1})	9.48
	I	368.28
3LA(M)	ω (cm^{-1})	395.25
	FWHM (cm^{-1})	11.69
	I	350.02

Table B.11 Parameters used for the fitting of T2 WSe_2.

Band	Parameter	Value
E'(Γ)	ω (cm^{-1})	246.23
	FWHM (cm^{-1})	4.74
	I	2110.97
A'_1(Γ)	ω (cm^{-1})	249.13
	FWHM (cm^{-1})	4.40
	I	2108.75
LA(M)+TA(M)	ω (cm^{-1})	238.29
	FWHM (cm^{-1})	11.11
	I	366.04
A''_2(M)	ω (cm^{-1})	258.62
	FWHM (cm^{-1})	10.98
	I	990.14
2LA(M)	ω (cm^{-1})	358.50
	FWHM (cm^{-1})	24.57
	I	114.98
LO_2(M)+LA(M)	ω (cm^{-1})	374.22
	FWHM (cm^{-1})	7.07
	I	226.72
3LA(M)	ω (cm^{-1})	395.33
	FWHM (cm^{-1})	8.77
	I	241.39

Table B.12 Parameters used for the fitting of T3 WSe_2.

Band	Parameter	Value
E'(Γ) / A'_1(Γ)	ω (cm^{-1})	248.42
	FWHM (cm^{-1})	6.53
	I	1156.87
LA(M)+TA(M)	ω (cm^{-1})	234.67
	FWHM (cm^{-1})	8.25
	I	109.81
	ω (cm^{-1})	240.31
	FWHM (cm^{-1})	4.51
	I	107.24
A''_2(M)	ω (cm^{-1})	257.96
	FWHM (cm^{-1})	10.88
	I	243.53
Not assigned yet	ω (cm^{-1})	307.45
	FWHM (cm^{-1})	5.99
	I	98.40
2LA(M)	ω (cm^{-1})	359.09
	FWHM (cm^{-1})	31.37
	I	70.72
LO_2(M)+LA(M)	ω (cm^{-1})	372.47
	FWHM (cm^{-1})	8.50
	I	84.35
3LA(M)	ω (cm^{-1})	393.47
	FWHM (cm^{-1})	9.96
	I	82.80